Effect of Solvent Diffusion on Crack-Tip Fields and Driving Force for Fracture of Hydrogels

Nikolaos Bouklas
Department of Aerospace Engineering and Engineering Mechanics, University of Texas, Austin, TX 78712

Chad M. Landis
Department of Aerospace Engineering and Engineering Mechanics, University of Texas, Austin, TX 78712

Rui Huang
Department of Aerospace Engineering and Engineering Mechanics, University of Texas, Austin, TX 78712

Hydrogels are used in a variety of applications ranging from tissue engineering to soft robotics. They often undergo large deformation coupled with solvent diffusion, and structural integrity is important when they are used as structural components. This paper presents a thermodynamically consistent method for calculating the transient energy release rate for crack growth in hydrogels based on a modified path-independent J-integral. The transient energy release rate takes into account the effect of solvent diffusion, separating the energy lost in diffusion from the energy available to drive crack growth. Numerical simulations are performed using a nonlinear transient finite element method for center-cracked hydrogel specimens, subject to remote tension under generalized plane strain conditions. The hydrogel specimen is assumed to be either immersed in a solvent or not immersed by imposing different chemical boundary conditions. Sharp crack and rounded notch models are used for small and large far-field strains, respectively. Comparisons to linear elastic fracture mechanics (LEFM) are presented for the crack-tip fields and crack opening profiles in the instantaneous and equilibrium limits. It is found that the stress singularity at the crack tip depends on both the far-field strain and the local solvent diffusion, and the latter evolves with time and depends on the chemical boundary conditions. The transient energy release rate is predicted as a function of time for the two types of boundary conditions with distinct behaviors due to solvent diffusion. Possible scenarios of delayed fracture are discussed based on evolution of the transient energy release rate. [DOI: 10.1115/1.4030587]

Keywords: fracture, J-integral, diffusion, soft material

1 Introduction

Hydrogel-like soft materials are abundant in nature including soft tissues such as cartilage, tendons, and ligaments. With similar mechanical properties and biocompatibility, synthetic hydrogels have been used extensively as biomaterials for a wide range of biomedical applications such as artificial soft tissues [1–3], extracellular matrix [4,5], and drug delivery [6]. More recently, hydrogel-like materials have been explored as a class of soft active materials with sensing and actuating properties in the development of soft machines and soft robotics [7–9]. Mechanical properties of the hydrogel-like soft materials are important for many of these applications. In particular, fracture of hydrogels has been studied by many, both for understanding the fracture mechanisms [10–14] and for characterizing the fracture properties such as toughness [15–19]. The distinct fracture mechanisms associated with different molecular structures have been exploited in recent developments of tough hydrogels [20–22]. The reported fracture toughness values for hydrogel-like soft materials range widely from $\sim 1\,\mathrm{J/m^2}$ for gelatin gels [18] to $\sim 1000\,\mathrm{J/m^2}$ for cartilage [16] and $\sim 9000\,\mathrm{J/m^2}$ for a hybrid alginate–polyacrylamide gel [21]. Several studies have noted the rate dependence of the fracture toughness [12–14,17–19], suggesting kinetic processes associated with fracture of hydrogels. Two primary suspects for the kinetic processes in hydrogel-like soft materials are polymer viscoelasticity and solvent diffusion [23]. The distinct time-dependent behaviors of hydrogels due to viscoelasticity and solvent diffusion (or poroelasticity) have been observed in recent compression and indentation experiments [24–26]. While fracture mechanics of viscoelastic materials has been studied extensively [27–31], the effects of solvent diffusion on fracture of hydrogels have received little attention until recently [32–34]. In this paper, we focus on the effects of solvent diffusion on fracture of hydrogels and ignore the effects of viscoelasticity.

The effects of solvent diffusion on fracture can be studied within the general framework of poroelasticity [35]. Similar problems have been studied in the field of geomechanics with applications in hydraulic fracture [36–38]. Unlike LEFM, where an elastic energy release rate is defined as the driving force for crack growth, the crack growth in a poroelastic material is accompanied by solvent diffusion that dissipates energy. Several previous works have considered the effect of solvent diffusion on the energy release rate based on conservation laws for thermo and poroelasticity [39–41]. More recently, Gao and Zhou [42] formulated a *J*-integral as the driving force for fracture in electrode materials of Li-ion batteries, with coupled mechanical deformation and mass diffusion processes under a steady-state condition. Haftbaradaran and Qu [43] constructed an electro-chemo-mechanical *J*-integral under equilibrium conditions without considering the kinetics of solute diffusion.

The main objective of this work is to develop a transient energy release rate as the driving force for crack growth in hydrogels based on a thermodynamic conservation law coupling the kinetics of solvent diffusion with large deformation. The effects of solvent diffusion on the transient energy release rate and the crack-tip fields are demonstrated by numerical simulations using a nonlinear transient finite element method. The remainder of this paper is organized as follows. Section 2 presents the derivation of a modified *J*-integral for the transient energy release rate, along with a domain integral method to calculate the *J*-integral. A specific

Contributed by the Applied Mechanics Division of ASME for publication in the Journal of Applied Mechanics. Manuscript received March 21, 2015; final manuscript received May 6, 2015; published online June 9, 2015. Editor: Yonggang Huang.

material model for hydrogels is outlined in Sec. 3, and a nonlinear transient finite element method is implemented with details of the formulation given in the Appendix B, a similar finite element method has been presented elsewhere [44]. The numerical results are discussed in Sec. 4, considering center-cracked hydrogel specimens subject to remote tension under generalized plane strain conditions. A sharp crack model is used first for small to moderately large far-field strains, and a rounded notch model is used for large far-field strains. Section 5 concludes the present study with a summary and discussion on delayed fracture of hydrogels.

2 General Formulation

2.1 A Nonequilibrium Thermodynamic Approach. Hydrogels in their simplest form consist of two components: long crosslinked polymer chains that form a three-dimensional network structure and small solvent molecules that can migrate within the network. The aggregate is then capable of large and reversible deformation subject to mechanical forces and/or environmental stimuli (e.g., humidity, temperature, etc). The nonlinear transient behavior of hydrogels with coupled deformation and solvent diffusion has been studied by many [45–49]. The general formulation by Hong et al. [46] is adopted in the present study.

The deformation of the aggregate can be traced by considering markers on the network with coordinates $\mathbf{X}$ in a reference configuration, which is chosen to coincide with the dry state of the hydrogel. In the current configuration, the markers are located with coordinates $\mathbf{x}$, and the deformation is characterized by the deformation gradient tensor $\mathbf{F}$ with Cartesian components, $F_{iJ} = \partial x_i/\partial X_J$. The nominal concentration of solvent C is defined as the number of solvent molecules per unit volume of the polymer network. The free energy density is taken to be a function of the deformation gradient and the solvent concentration, $U(\mathbf{F}, C)$. The nominal stress and the chemical potential are then obtained as thermodynamic work conjugates by

$$s_{iJ}(\mathbf{F}, \mathrm{C}) = \frac{\partial U}{\partial F_{iJ}} \tag{2.1}$$

$$\mu(\mathbf{F}, \mathrm{C}) = \frac{\partial U}{\partial C} \tag{2.2}$$

Mechanical equilibrium is maintained during the transient processes so that

$$\frac{\partial s_{iJ}}{\partial X_J} + b_i = 0 \text{ in } V_0 \tag{2.3}$$

$$s_{iJ}N_J = T_i \text{ on } S_0 \tag{2.4}$$

where b_i is the nominal body force (per unit volume), V_0 and S_0 are the body and its boundary in the reference configuration, respectively, N_J is the outward unit normal on the boundary of the reference configuration, and T_i is the nominal traction on the boundary.

Conservation of solvent molecules leads to a rate equation for the solvent concentration

$$\frac{\partial C}{\partial t} + \frac{\partial J_K}{\partial X_K} = r \text{ in } V_0 \tag{2.5}$$

$$J_K N_K = -i \text{ on } S_0 \tag{2.6}$$

where J_K is the nominal flux of solvent, defined as the number of solvent molecules crossing unit reference area per unit time, r is a source term for the number of solvent molecules injected into unit reference volume per unit time, and i is the inward flux rate across the boundary. The chemical boundary condition for the gel often can be prescribed with specified solvent flux or chemical potential.

There are two ways to do work on the hydrogel aggregate. One is by the application of mechanical forces, including body forces and surface tractions. The second is the exchange of solvent molecules through the source or the surface flux. Following the approach of nonequilibrium thermodynamics [50,51], the total potential energy of the aggregate system Π can be written as a sum of the internal stored energy and the work of the external mechanisms, and then the rate of the total potential energy is

$$\frac{d\Pi}{dt} = \int_{V_0} \frac{dU}{dt} dV - \int_{V_0} b_i \frac{dx_i}{dt} dV - \int_{S_0} T_i \frac{dx_i}{dt} dS - \int_{V_0} \mu r dV - \int_{S_0} \mu i dS \tag{2.7}$$

With Eqs. (2.1)–(2.6), the rate of the potential energy reduces to

$$\frac{d\Pi}{dt} = \int_{V_0} J_K \frac{\partial \mu}{\partial X_K} dV \tag{2.8}$$

For an isothermal process, the second law of thermodynamics dictates that

$$\frac{d\Pi}{dt} \le 0 \tag{2.9}$$

For Eq. (2.9) to hold in any arbitrary part of the body, it is required that

$$J_K \frac{\partial \mu}{\partial X_K} \le 0 \text{ in } V_0 \tag{2.10}$$

This imposes a constraint on the kinetics relating the nominal flux to the gradient of chemical potential. A specific form of the kinetics is adopted for numerical simulations as described in Sec. 3.

By Eq. (2.8), the change of the total potential energy is solely related to the energy dissipation associated with solvent diffusion. The rate of energy dissipation is then

$$\frac{d\Sigma}{dt} = -\int_{V_0} J_K \frac{\partial \mu}{\partial X_K} dV \tag{2.11}$$

In terms of the accumulative flux, $I_K = \int_0^t J_K dt$, the rate of energy dissipation can be written as

$$\frac{d\Sigma}{dt} = -\int_{V_0} \frac{\partial \mu}{\partial X_K} \frac{dI_K}{dt} dV \tag{2.12}$$

The total energy of the system can be defined as the sum of the potential energy and the energy dissipation due to solvent diffusion, namely,

$$\Psi = \Pi + \Sigma \tag{2.13}$$

By definition, we have conservation of the total energy $d\Psi/dt = 0$ throughout the transient stage (without crack growth for the moment). Equivalently, the variation of the total energy must vanish at any time, i.e.,

$$\delta\Psi = \int_{V_0} \left(\delta U - \frac{\partial \mu}{\partial X_K} \delta I_K - b_i \delta x_i - \mu r \delta t \right) dV - \int_{S_0} (T_i \delta x_i - \mu N_K \delta I_K) dS = 0 \tag{2.14}$$

2.2 Transient Energy Release Rate. Next, we derive the energy release rate for quasistatic crack growth in a hydrogel,

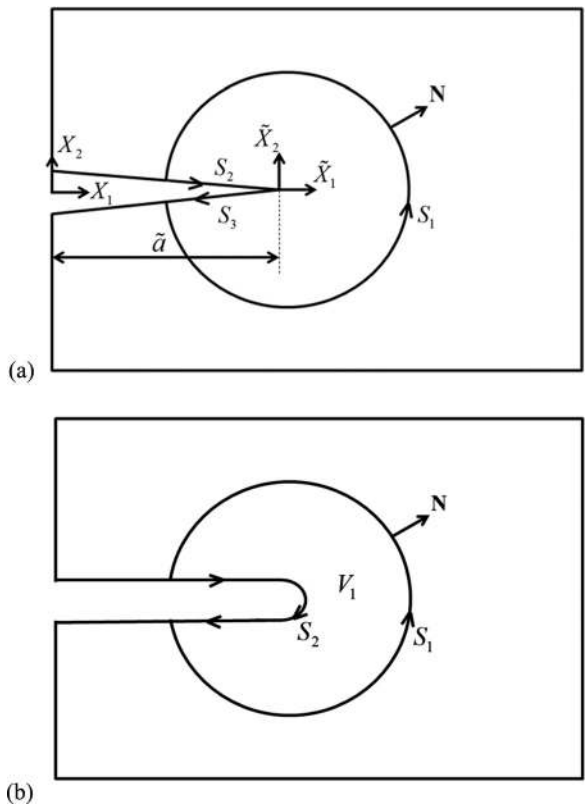

Fig. 1 Schematics of (*a*) a sharp crack and (*b*) a rounded notch model, both in the reference configuration

where the inertial effect is negligible and the crack growth is slow in terms of the time scale of solvent diffusion (including the case of a stationary crack). Consider a hydrogel body that contains a crack of length a in the current configuration. In the corresponding reference configuration (Fig. 1(*a*)), the crack length is denoted as $\tilde{a}$, $\mathbf{X}$ refers to a fixed coordinate system, and $\tilde{\mathbf{X}}$ refers to a moving coordinate system with its origin at the crack tip. For convenience, the two coordinate systems are set such that $\tilde{X}_1 = X_1 - \tilde{a}$ and $\tilde{X}_2 = X_2$ (assuming crack growth in the X_1 direction). Growth of the crack in the hydrogel is accompanied by deformation of the polymer network and migration of the solvent molecules. As a result, the change of total potential energy includes a conservative part and a dissipative part. The driving force for crack growth is the release of the total energy Ψ. Following Eq. (2.14), the rate of total energy change with respect to the crack length is

$$\frac{d\Psi}{d\tilde{a}} = \int_{V_0}\left(\frac{dU}{d\tilde{a}} - \frac{\partial\mu}{\partial X_K}\frac{dI_K}{d\tilde{a}}\right)dV - \int_{S_0}\left(T_i\frac{dx_i}{d\tilde{a}} - \mu N_K\frac{dI_K}{d\tilde{a}}\right)dS \tag{2.15}$$

where $S_0 = S_1 + S_2 + S_3$ in Fig. 1(*a*); the body force and solvent injection source have been ignored hereafter. The derivation of Eq. (2.15) is given in Appendix A.

With respect to the fixed coordinate $\mathbf{X}$ in the reference configuration, we have

$$\frac{d}{d\tilde{a}} = \frac{\partial}{\partial\tilde{a}} + \frac{\partial\tilde{X}_1}{\partial\tilde{a}}\frac{\partial}{\partial\tilde{X}_1} = \frac{\partial}{\partial\tilde{a}} - \frac{\partial}{\partial\tilde{X}_1} = \frac{\partial}{\partial\tilde{a}} - \frac{\partial}{\partial X_1} \tag{2.16}$$

where the spatial derivatives are taken at constant $\tilde{a}$. Hence, the rate of the total energy change becomes

$$\frac{d\Psi}{d\tilde{a}} = \int_{V_0}\left(\frac{\partial U}{\partial\tilde{a}} - \frac{\partial U}{\partial X_1}\right)dV - \int_{S_0} s_{iJ}N_J\left(\frac{\partial x_i}{\partial\tilde{a}} - \frac{\partial x_i}{\partial X_1}\right)dS + \int_{S_0}\mu N_K\left(\frac{\partial I_K}{\partial\tilde{a}} - \frac{\partial I_K}{\partial X_1}\right)dS - \int_{V_0}\frac{\partial\mu}{\partial X_K}\left(\frac{\partial I_K}{\partial\tilde{a}} - \frac{\partial I_K}{\partial X_1}\right)dV \tag{2.17}$$

Considering the first term on the right-hand side of Eq. (2.17), with Eqs. (2.1) and (2.2), we obtain that

$$\int_{V_0}\frac{\partial U}{\partial\tilde{a}}dV = \int_{V_0}\left(s_{iJ}\frac{\partial F_{iJ}}{\partial\tilde{a}} + \mu\frac{\partial C}{\partial\tilde{a}}\right)dV \tag{2.18}$$

By integrating Eq. (2.5) over time with $r = 0$ (no solvent injection), the solvent concentration is obtained as

$$C - C_0 + \frac{\partial I_K}{\partial X_K} = 0 \tag{2.19}$$

where C_0 is the nominal concentration at the initial state ($t = 0$) of the hydrogel. The initial state does not have to coincide with the dry state (reference). It is often taken as a free swollen state with a homogeneous solvent concentration and an isotropic deformation gradient, $F_{11} = F_{22} = F_{33} = \lambda_0$. With Eqs. (2.19), (2.3), and (2.4), applying the divergence theorem, Eq. (2.18) becomes

$$\int_{V_0}\frac{\partial U}{\partial\tilde{a}}dV = \int_{S_0}\left(s_{iJ}N_J\frac{\partial x_i}{\partial\tilde{a}} - \mu N_K\frac{\partial I_K}{\partial\tilde{a}}\right)dS + \int_{V_0}\frac{\partial\mu}{\partial X_K}\frac{\partial I_K}{\partial\tilde{a}}dV \tag{2.20}$$

Inserting Eq. (2.20) back into Eq. (2.17), we obtain the transient energy release rate in form of a modified J-integral as

$$J^* = -\frac{d\Psi}{d\tilde{a}} = \int_{S_0}\left(UN_1 - s_{iJ}N_J\frac{\partial x_i}{\partial X_1} + \mu N_K\frac{\partial I_K}{\partial X_1}\right)dS - \int_{V_0}\frac{\partial\mu}{\partial X_K}\frac{\partial I_K}{\partial X_1}dV \tag{2.21}$$

A more convenient form of the modified J-integral is obtained by combining the flux terms with the relation in Eq. (2.19) so that

$$J^* = \int_{S_1}\left(UN_1 - s_{iJ}N_J\frac{\partial x_i}{\partial X_1}\right)dS - \int_{V_0}\mu\frac{\partial C}{\partial X_1}dV \tag{2.22}$$

where the initial solvent concentration has been assumed to be homogeneous (or $\partial C_0/\partial X_1 = 0$) and the traction-free condition on the crack surfaces (S_2 and S_3 in Fig. 1(*a*)) has been used to simplify the first integral on the right-hand side. It can be shown that, for a simply connected domain without singularities, the modified J-integral is necessarily zero by the mechanical equilibrium and mass conservation conditions in Eqs. (2.1)–(2.6). For a domain containing a crack tip (Fig. 1(*a*)), the modified J-integral is path-independent, giving the transient energy release rate for straight-ahead crack growth in the X_1 direction.

Alternatively, by using Legendre transform of the free energy density function

$$\hat{U}(\mathbf{F},\mu) = U(\mathbf{F},C) - \mu C \tag{2.23}$$

the modified J-integral can be rewritten as

$$J^* = \int_{S_1}\left(\hat{U}N_1 - s_{iJ}N_J\frac{\partial x_i}{\partial X_1}\right)dS + \int_{V_0}\frac{\partial\mu}{\partial X_1}CdV \tag{2.24}$$

which is used for the rest of this study. The form of the modified J-integral in Eq. (2.24) is preferable for numerical calculations

in the finite element framework, because it does not require calculating the derivatives of the solvent concentration, which would usually require higher order interpolations [44,49].

We note that the modified J-integral in Eq. (2.24) has two parts: a surface integral, similar to the classic definition of J-integral [52], and in addition, a volume integral containing the gradient of chemical potential. This form of J-integral is similar to those for fracture of battery electrodes with solute diffusion as obtained by Gao and Zhou [42] under a steady-state condition. Similar integrals were also obtained for hygro-thermo-elastic fracture [39,41]. We note that, by using the Legendre transform of the free energy function, the volume integral in Eq. (2.24) vanishes in the equilibrium state (with constant μ). However, using the original free energy function, the volume integral in Eq. (2.22) remains unless $\mu = 0$.

The modified J-integral can be used to calculate the transient energy release rate for a sharp crack model (Fig. 1(*a*)) using a contour around the crack tip, similar to the classic J-integral [52,53]. In a blunt crack model with a rounded notch at the crack tip (Fig. 1(*b*)), the integral has to be modified slightly to account for the initial free energy at the notch, as further discussed in Sec. 4.2.

2.3 Domain Integral Method. For an accurate calculation of the standard J-integral by the finite element method, it is advantageous to convert the surface integral to a volume integral. This procedure is known as the domain integral method. The approach of Li et al. [54] is adopted in the present study for the two-dimensional case to convert the contour integral into a domain integral to calculate the transient energy release rate for quasi-static crack growth in hydrogels. Considering an annular region around the crack tip in the reference configuration, as shown in Fig. 2, the transient energy release rate for a sharp crack can be obtained from the modified J-integral with the contour C_1 and the enclosed domain A_1 as

$$J^* = \int_{C_1} \left(\hat{U} N_1 - s_{iJ} N_J \frac{\partial x_i}{\partial X_1} \right) d\Gamma + \int_{A_1} \frac{\partial \mu}{\partial X_1} C dA \tag{2.25}$$

Now consider a closed contour $C = C_4 - C_1 + C_2 + C_3$ bounding the annular area A_2. Denote $\tilde{\mathbf{N}}$ as the outward normal on C with respect to A_2, which coincides with $\mathbf{N}$ on C_3, but is opposite to $\mathbf{N}$ on C_1. The J-integral in Eq. (2.25) can then be rewritten with a closed contour integral as

$$J^* = -\oint_C \left(\hat{U} \tilde{N}_1 - s_{iJ} \tilde{N}_J \frac{\partial x_i}{\partial X_1} \right) q d\Gamma + \int_{A_1} \frac{\partial \mu}{\partial X_1} C q dA \tag{2.26}$$

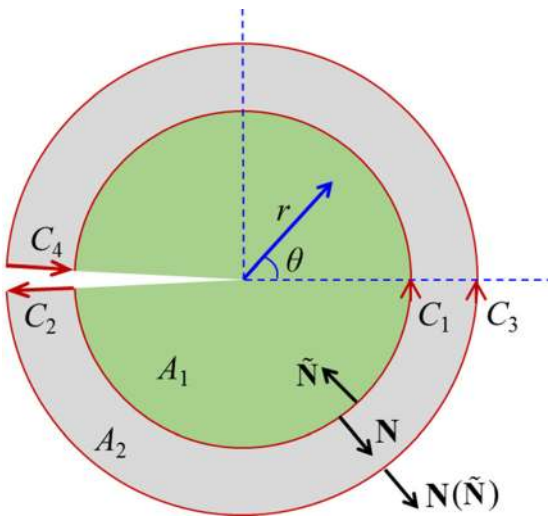

Fig. 2 A simply connected region A_2 enclosed by a closed contour $C = C_4 - C_1 + C_2 + C_3$ around a crack tip

where q is a sufficiently smooth function in A_2, varying from unity on C_1 to zero on C_3. In addition, we set $q = 1$ in A_1. Note that the contour integrals along the crack faces (C_2 and C_4) vanish because they are assumed to be traction free and $N_1 = 0$ (for a straight crack). Since the area A_2 is simply connected without any singularities, we apply the divergence theorem on the closed contour integral in Eq. (2.26) and obtain that

$$J^* = -\int_{A_2} \left(\hat{U} \frac{\partial q}{\partial X_1} - s_{iJ} F_{i1} \frac{\partial q}{\partial X_J} \right) dA + \int_{A_1 + A_2} \frac{\partial \mu}{\partial X_1} C q dA \tag{2.27}$$

which is similar to the domain integral obtained by Li et al. [54] but includes an additional term associated with solvent diffusion. We note that the additional term vanishes when the hydrogel reaches chemical equilibrium with a constant chemical potential or when $C = 0$ for the dry state. As demonstrated in Sec. 4, the domain integral in Eq. (2.27) is convenient for numerical calculations using the finite element method.

3 A Specific Material Model and Finite Element Method

In this section, a specific material model is presented for hydrogels, and a nonlinear finite element method to solve initial boundary value problems is outlined. The finite element method is similar to that in a previous study [44], but with some variations due to a slightly different material model. For completeness, the detailed finite element formulation is presented in Appendix B.

Following Hong et al. [46], a free energy density function based on the Flory–Rehner theory is adopted, which takes the form

$$U(\mathbf{F}, C) = U_e(\mathbf{F}) + U_m(C) \tag{3.1}$$

where

$$U_e(\mathbf{F}) = \frac{1}{2} N k_B T [F_{iK} F_{iK} - 3 - 2 \ln(\det(\mathbf{F}))] \tag{3.2}$$

$$U_m(C) = \frac{k_B T}{\Omega} \left(\Omega C \ln \frac{\Omega C}{1 + \Omega C} + \frac{\chi \Omega C}{1 + \Omega C} \right) \tag{3.3}$$

The free energy density is proportional to the thermal energy $k_B T$, with Boltzmann constant k_B and absolute temperature T. In addition, it depends on the effective number density of polymer chains in the dry state (N), the molecular volume of the solvent (Ω), and the Flory parameter (χ) for the polymer–solvent interaction.

The constituents of the hydrogel are assumed to be incompressible so that the volume of the hydrogel is a simple sum of the volume of polymer and the volume of solvent. As such, the determinant of the deformation gradient is related to the nominal solvent concentration as

$$\det(\mathbf{F}) = 1 + \Omega C \tag{3.4}$$

This is different from the previous study in Ref. [44] where a finite compressibility was assumed. With Eq. (3.4), the solvent concentration is calculated explicitly as a function of the deformation gradient. This calculation is simpler than that in Bouklas et al. [44] where the solvent concentration had to be calculated by solving a nonlinear algebraic equation at each integration point.

With Eqs. (3.1)–(3.4), the Legendre transform of the free energy density function in Eq. (2.23) becomes

$$\begin{aligned} \hat{U}(\mathbf{F}, \mu) = {} & \frac{1}{2} N k_B T [F_{iK} F_{iK} - 3 - 2 \ln(\det(\mathbf{F}))] + \\ & + \frac{k_B T}{\Omega} \left[(\det(\mathbf{F}) - 1) \ln \frac{(\det(\mathbf{F}) - 1)}{\det(\mathbf{F})} + \frac{\chi (\det(\mathbf{F}) - 1)}{\det(\mathbf{F})} \right] \\ & - \frac{\mu (\det(\mathbf{F}) - 1)}{\Omega} \end{aligned} \tag{3.5}$$

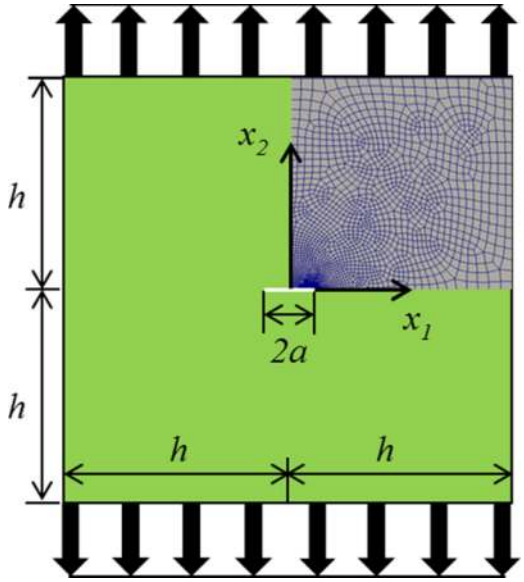

Fig. 3 A hydrogel specimen with a center crack, subject to remote tension. A two-dimensional finite element mesh for one quarter of the specimen is shown.

The nominal stress is then obtained as

$$s_{iJ} = \frac{\partial \hat{U}}{\partial F_{iJ}} = Nk_BT(F_{iJ} + \alpha H_{iJ}) \tag{3.6}$$

where

$$\alpha = -\frac{1}{\det \mathrm{F}} + \frac{1}{N\Omega}\left(\ln\frac{\det \mathrm{F}-1}{\det \mathrm{F}} + \frac{1}{\det \mathrm{F}} + \frac{\chi}{(\det \mathrm{F})^2} - \frac{\mu}{k_BT}\right) \tag{3.7}$$

$$H_{iJ} = \frac{1}{2}e_{ijk}e_{JKL}F_{jK}F_{kL} \tag{3.8}$$

To study the transient behavior of a hydrogel, a kinetic law has to be assumed for solvent migration. Based on a diffusion model adopted by Hong et al. [46], the nominal flux takes the form

$$J_K = -M_{KL}\frac{\partial \mu}{\partial X_L} \tag{3.9}$$

with a nominal mobility tensor

$$M_{KL} = \frac{DC}{k_BT}\left(\frac{\partial X_K}{\partial x_k}\frac{\partial X_L}{\partial x_k}\right) \tag{3.10}$$

where D is a constant for solvent diffusivity.

The constitutive relations in Eqs. (3.4)–(3.6) and the kinetic law in Eq. (3.9), along with Eqs. (2.3) and (2.4) for mechanical equilibrium and Eqs. (2.5) and (2.6) for mass conservation as well as the corresponding initial and boundary conditions, complete the strong form of the initial boundary value problem. The initial conditions are typically described by a displacement field ($\mathbf{u} = \mathbf{x} - \mathbf{X}$) and chemical potential

$$\mathbf{u}|_{t=0} = \mathbf{u}_0 \tag{3.11}$$

$$\mu|_{t=0} = \mu_0 \tag{3.12}$$

Relative to the dry state ($\mu \to -\infty$), the initial displacement field can be prescribed for a homogeneous deformation corresponding to a constant chemical potential (e.g., $\mu_0 = 0$). At $t = 0^+$, the boundary conditions are applied and the hydrogel undergoes a transient process with coupled deformation and solvent diffusion.

The weak form, time integration, and spatial discretization for the finite element method are presented in Appendix B. As discussed previously in Bouklas et al. [44], the incompressible or nearly incompressible behavior of the hydrogel at the instantaneous limit ($t \to 0$) poses a numerical issue for convergence and stability, similar to those for the mixed finite element methods in linear poroelasticity [55–57]. To obtain numerically stable results, Taylor–Hood elements [58] are used, where interpolation for chemical potential is one order lower than for displacement. In particular, the lowest order Taylor–Hood element that produces stable results is implemented using quadratic shape functions (eight nodes) for the displacement and linear shape functions (four nodes) for the chemical potential (i.e., 8u4p). The corresponding singular element (6u3p) at a sharp crack tip is implemented with six nodes for the displacement (including two quarter-point nodes) and three nodes for the chemical potential.

4 Numerical Results and Discussion

In this section, we consider a hydrogel specimen with a center crack (Fig. 3), subject to remote tension by Mode I displacement controlled loading under generalized plane strain conditions. Different boundary conditions are used to simulate hydrogels either immersed in a solvent or not immersed. By symmetry, only a quarter of the rectangular domain is modeled with a

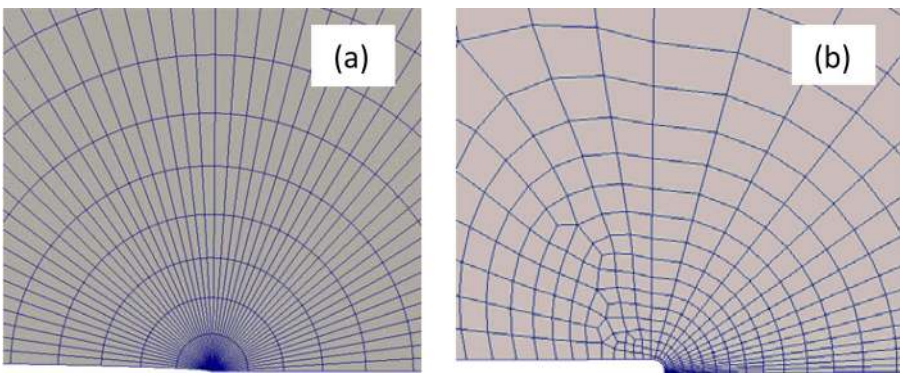

Fig. 4 (*a*) Finite element mesh near the crack tip in the sharp crack model, with 50 quarter-point singular Taylor–Hood elements (6u3p). (*b*) Mesh near a rounded notch, where the radius of the notch is three orders of magnitude smaller than the crack length ($r_n/a = 10^{-3}$).

two-dimensional finite element mesh. A sharp crack model is used for the cases with infinitesimal to moderately large far-field deformation, whereas a rounded notch model is used for the cases with generally large far-field deformation. The sharp crack model (Fig. 4(*a*)) uses collapsed quarter-point Taylor–Hood elements (6u3p) around the crack tip along with the quadrilateral Taylor–Hood elements (8u4p) for the rest of the model. The rounded notch model (Fig. 4(*b*)) uses the quadrilateral Taylor–Hood elements throughout.

In the initial state ($t=0$), the hydrogel is fully swollen and stress free, characterized by a homogeneous swelling ratio λ_0 corresponding to an initial chemical potential, $\mu_0 = 0$. The initial swelling ratio depends on the material properties of the hydrogel, which can be determined by solving a nonlinear algebraic equation [59]

$$\ln\frac{\lambda_0^3-1}{\lambda_0^3}+\frac{1}{\lambda_0^3}+\frac{\chi}{\lambda_0^6}+N\Omega\left(\frac{1}{\lambda_0}-\frac{1}{\lambda_0^3}\right)=\frac{\mu_0}{k_BT} \tag{4.1}$$

Relative to the dry state, the initial displacement is $\mathbf{u}_0 = \lambda_0\mathbf{X} - \mathbf{X}$. The crack length in the initial state is $2a$, and the height and width of the rectangular specimen are both $2h$ ($h = 10a$). In the corresponding reference state, the crack length is $2\tilde{a}$ ($\tilde{a} = a/\lambda_0$). The dimensionless material parameters, $N\Omega = 10^{-3}$ and $\chi = 0.2$, are used throughout this section (unless noted otherwise), giving rise to an initial swelling ratio $\lambda_0 = 3.215$.

Referring to the coordinates in Fig. 3, the symmetry boundary conditions are imposed as

$$\Delta u_1|_{x_1=0}=0,\quad s_{21}|_{x_1=0}=0,\quad J_1|_{x_1=0}=0 \tag{4.2}$$

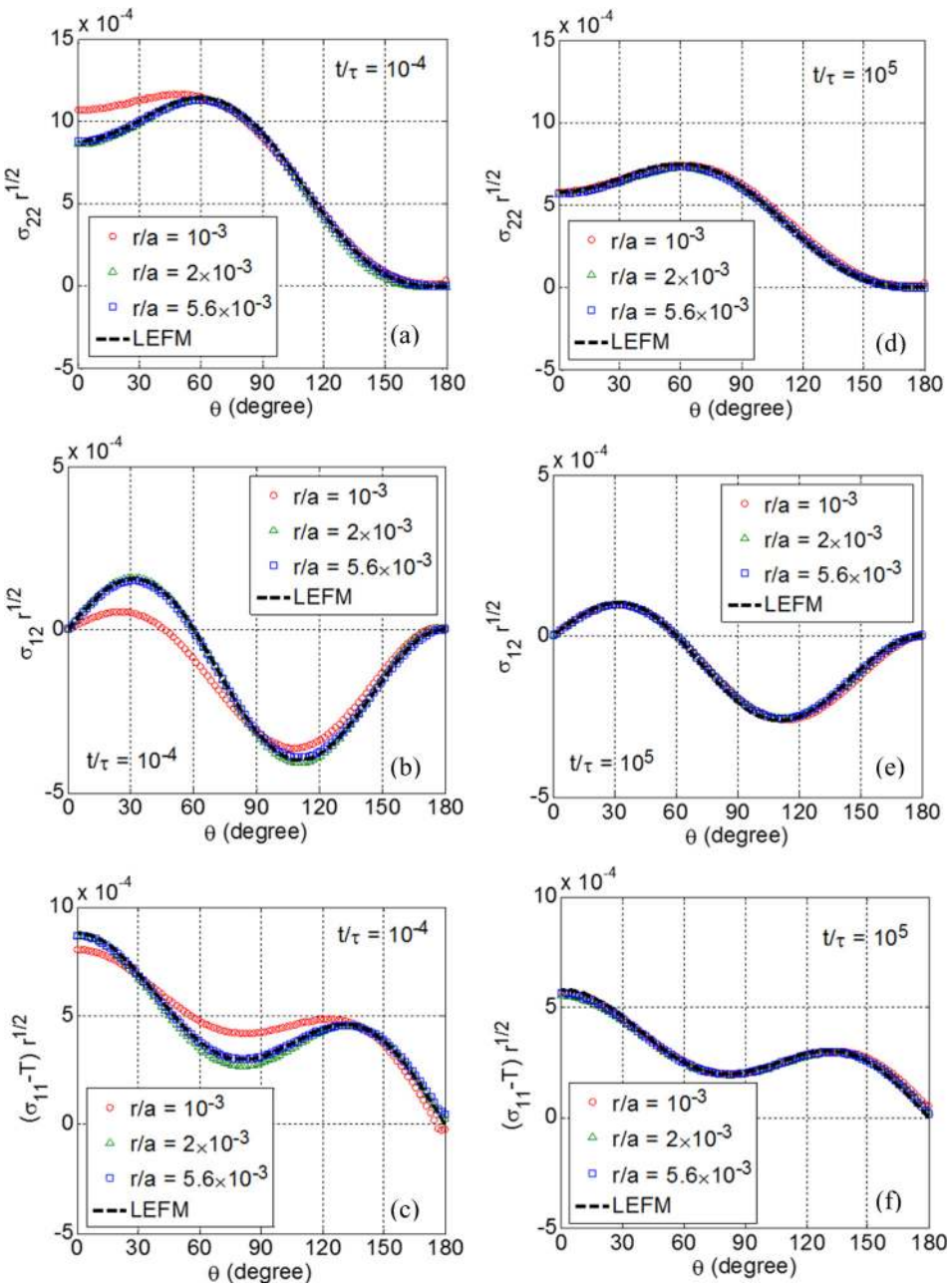

Fig. 5 Cauchy stress distributions around a crack tip at the instantaneous ((*a*)–(*c*)) and equilibrium ((*d*)–(*f*)) limits for an immersed hydrogel specimen under Mode I loading ($\varepsilon_\infty = 10^{-3}$), with increasing distance (r) from the crack tip. Dashed lines are obtained from the LEFM solution in Eq. (4.7) with Poisson's ratio $\nu = 0.5$ and 0.2415, respectively, for the two limits.

and

$$\Delta u_2|_{\substack{x_2=0\\x_1>a}} = 0, \quad s_{12}|_{\substack{x_2=0\\x_1>a}} = 0, \quad J_2|_{\substack{x_2=0\\x_1>a}} = 0 \tag{4.3}$$

where $\Delta\mathbf{u} = \mathbf{u} - \mathbf{u}_0$.

The remote tension is applied through a mixed boundary condition at $x_2 = h$

$$\Delta u_2|_{x_2=h} = \varepsilon_\infty h \text{ and } s_{12}|_{x_2=h} = 0 \tag{4.4}$$

The far-field deformation is thus characterized by uniaxial tension with a nominal strain ε_∞. The crack face and the other boundary at $x_1 = h$ are traction free. In the case of a hydrogel immersed in solvent, the chemical potential at the crack face and the outer boundaries is set by the local equilibrium condition as

$$\mu|_{\substack{x_2=0\\x_1<a}} = \mu|_{x_2=h} = \mu|_{x_1=h} = 0 \tag{4.5}$$

On the other hand, if the hydrogel is not immersed in solvent, we assume no-flux boundary condition on the crack face and the outer boundaries

$$J_2|_{\substack{x_2=0\\x_1<a}} = J_2|_{x_2=h} = J_1|_{x_1=h} = 0 \tag{4.6}$$

For convenience, dimensionless quantities are defined as follows: all lengths are normalized by the crack length (a), time is normalized by the characteristic diffusion time scale, $\tau = a^2/D$, stresses are normalized by Nk_BT, chemical potential by k_BT, and solvent concentration by Ω^{-1}.

4.1 Sharp Crack Model

4.1.1 Small Far-Field Deformations. Subject to a small far-field strain (i.e., $\varepsilon_\infty = 10^{-3}$), the stress field around the crack tip can be compared to the well-known result from LEFM [60]

$$\sigma_{ij}(r,\theta) = \frac{K_I}{\sqrt{2\pi r}} f_{ij}^I(\theta) + T\delta_{1i}\delta_{1j} \tag{4.7}$$

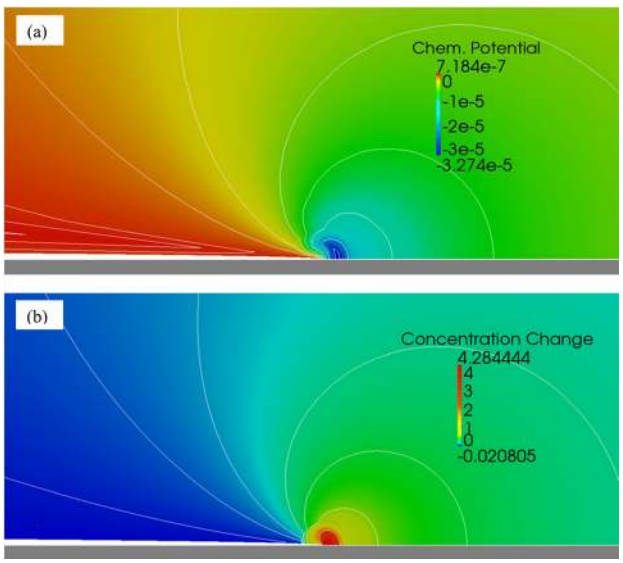

Fig. 6 (*a*) Chemical potential field (normalized as μ/k_BT) near the crack tip as the instantaneous response ($t/\tau = 10^{-4}$) of the hydrogel subject to a small remote strain ($\varepsilon_\infty = 10^{-3}$). (*b*) Change of solvent concentration (normalized as $(C - C_0)\Omega$) near the crack tip in the equilibrium state ($t/\tau = 10^5$).

where K_I is the stress intensity factor and

$$\begin{aligned} f_{11}^I &= \cos\frac{\theta}{2}\left(1 - \sin\frac{\theta}{2}\sin\frac{3\theta}{2}\right) \\ f_{12}^I &= \cos\frac{\theta}{2}\sin\frac{\theta}{2}\cos\frac{3\theta}{2} \\ f_{22}^I &= \cos\frac{\theta}{2}\left(1 + \sin\frac{\theta}{2}\sin\frac{3\theta}{2}\right) \end{aligned} \tag{4.8}$$

Here, (r, θ) is the local polar coordinate in the current configuration with $r = 0$ at the crack tip and $\theta = 0$ at $x_2 = 0$ for $x_1 > a$ (see Fig. 2). For the center-crack specimen, $K_I = \sigma_\infty\sqrt{\pi a}$ and $T = -\sigma_\infty$, where σ_∞ is the far-field stress.

For an immersed hydrogel specimen, the far-field stress is $\sigma_\infty = 2G\varepsilon_\infty/(1-\nu)$, which is a function of time [61]. Based on the linearized constitutive relations [59], the effective shear modulus of the swollen hydrogel is

$$G = \frac{Nk_BT}{\lambda_0} \tag{4.9}$$

while the effective Poisson's ratio is 0.5 (incompressible) for the instantaneous response ($t \to 0$) and is less than 0.5 in the equilibrium state ($t \to \infty$). Therefore, the instantaneous stress intensity factor is expected to be greater than the equilibrium value for

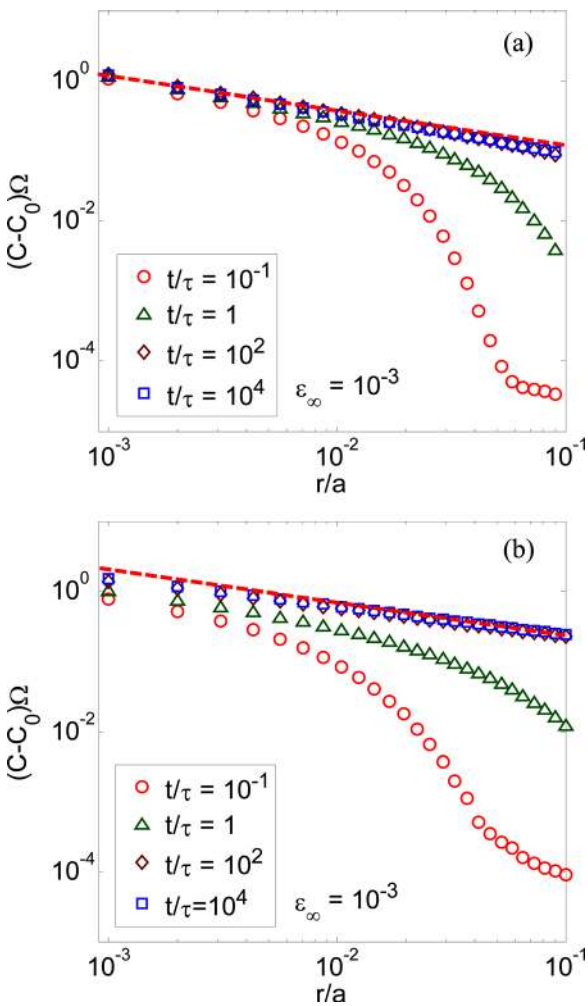

Fig. 7 Change of solvent concentration ahead of the crack tip for (*a*) an immersed and (*b*) a not-immersed hydrogel specimens subject to a small remote strain ($\varepsilon_\infty = 10^{-3}$). The dashed line has a slope of −0.5 in the log–log scale.

the immersed hydrogel specimen subject to a constant far-field strain ε_∞. The equilibrium Poisson's ratio is related to the intrinsic properties of the hydrogel by [59]

$$\nu_\infty = \frac{1}{2} - \frac{N\Omega}{2}\left[\frac{1}{\lambda_0^2(\lambda_0^3-1)} + \frac{N\Omega}{\lambda_0^2} - \frac{2\chi}{\lambda_0^5}\right]^{-1} \tag{4.10}$$

which gives $\nu_\infty = 0.2415$ for the specific material parameters ($N\Omega = 10^{-3}$ and $\chi = 0.2$).

Figure 5 shows the instantaneous and equilibrium stress distributions around the crack tip for an immersed hydrogel specimen with $\varepsilon_\infty = 10^{-3}$. To examine the nature of stress singularity at the crack tip, the Cauchy stress components, $\sigma_{ij} = s_{iK}F_{jK}/\det(\mathbf{F})$, are rescaled as $\sigma_{ij}\sqrt{r/a}/(Nk_BT)$ and plotted as functions of the angle θ at locations with increasing distance (r) from the crack tip, with the T-stress ($T = -\sigma_\infty$) subtracted from σ_{11}. The instantaneous limit ($t \to 0$) is taken approximately at $t/\tau = 10^{-4}$, and the equilibrium limit ($t \to \infty$) is taken at $t/\tau = 10^5$. In both limits, the rescaled stress components are in close agreement with the LEFM solution (Eq. (4.7)), but with different stress intensity factors due to the change of Poisson's ratio as a result of solvent diffusion (poroelastic relaxation). Except for the first ring very close to the crack tip ($r/a = 10^{-3}$), the rescaled stress components are independent of the distance r, confirming a square-root stress singularity near the crack tip. The results from the first ring of elements slightly deviate from the rest for the instantaneous response. This may be attributed to numerical oscillations caused by the discontinuity of the chemical potential on the boundary at the instantaneous limit, as discussed in a previous study [44]. Briefly, as the system is loaded at $t = 0^+$, the chemical potential changes instantaneously to a value different from the boundary condition along the crack face, which creates a discontinuity of the chemical potential at the boundary and cannot be resolved exactly by the finite element method. The numerical oscillations dissipate over time and have no effect on the equilibrium state.

If the hydrogel specimen is not immersed in solvent, the total volume is conserved although internal solvent diffusion may result in local volume change, mostly around the crack tip [33]. In this case, it is found that the stress field around the crack tip subject to a small far-field strain ($\varepsilon_\infty = 10^{-3}$) is close to the LEFM solution with $\nu = 0.5$ at both the instantaneous and equilibrium limits [62]. Therefore, the stress intensity factors at the two limits are nearly identical. However, as discussed later in this section, the instantaneous and equilibrium energy release rates calculated by the modified J-integral are different. Apparently, due to the effect of solvent diffusion around the crack tip, the LEFM relationship between the stress intensity factor and the energy release rate (i.e., $J = K^2/E$) is no longer applicable for the hydrogel specimen.

At $t \to 0$, the instantaneous deformation of the hydrogel results in an inhomogeneous field of chemical potential around the crack

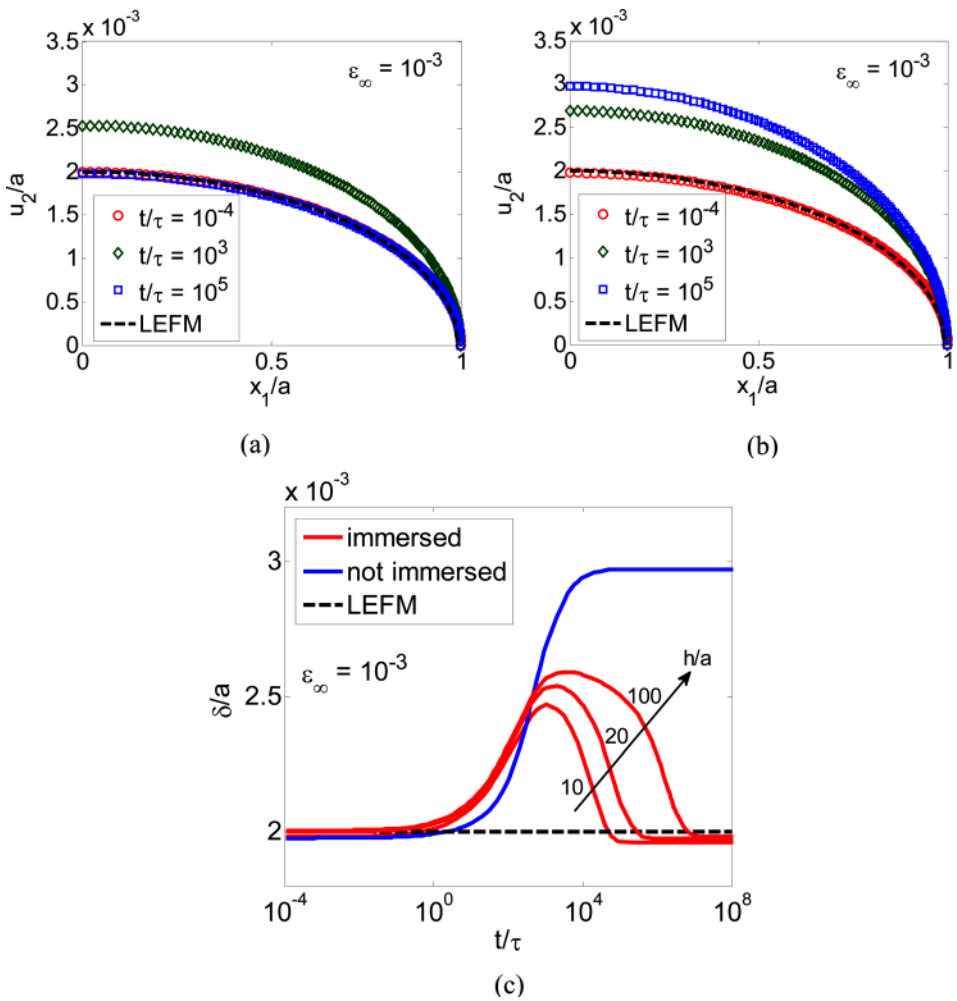

Fig. 8 Crack opening profiles for (*a*) immersed and (*b*) not-immersed hydrogel specimens subject to a small remote strain ($\varepsilon_\infty = 10^{-3}$). (*c*) Maximum crack opening displacement as a function of time for the two cases. Dashed lines are the LEFM solution as given in Eq. (4.11).

(Fig. 6(*a*)) while the solvent concentration remains homogeneous. The gradient of the chemical potential drives solvent diffusion, resulting in an inhomogeneous field of solvent concentration in the transient stage and the equilibrium state (Fig. 6(*b*)). In the immersed case, the boundary condition dictates that the chemical potential is zero at the crack face including the crack tip, while the chemical potential ahead of the crack tip first decreases and then increases with the distance. Thus, the solvent migrates toward the location with the minimum chemical potential, slightly ahead of the crack tip. Moreover, along the crack face, the gradient of chemical potential drives diffusion of solvent into the crack (out of the hydrogel body). At equilibrium, the chemical potential becomes zero everywhere, but the solvent concentration is higher at the crack tip but lower along the crack face (Fig. 6(*b*)). In the not-immersed case, the instantaneous chemical potential field is similar, with the minimum at the crack tip [62]. With the no-flux boundary condition at the crack face, the solvent diffusion can only redistribute the solvent concentration within the hydrogel around the crack tip. At equilibrium, the chemical potential is a constant everywhere, but with a value slightly lower than zero.

As a result of solvent diffusion, the concentration field evolves with time. At the instantaneous limit ($t \to 0$), the volumetric strain with respect to the initial state is expected to be zero (incompressible) and hence $C(t \to 0) \approx C_0$. Driven by the gradient of chemical potential, solvent diffusion leads to a singular volumetric strain associated with the solvent concentration. As shown in Fig. 7, the normalized change of solvent concentration, $(C - C_0)\Omega$, approaches the square-root singularity for both the immersed and not-immersed cases. In the LEFM solution, the volumetric strain follows the square-root singularity as long as the material is compressible ($\nu < 0.5$). Hence, the same singularity is expected for the solvent concentration at the equilibrium state ($t \to \infty$ and $\nu_\infty = 0.2415$) for the immersed case. However, for the not-immersed case, such a singularity cannot be explained by LEFM. With solvent diffusion around the crack tip, the hydrogel can no longer be treated as a homogenous elastic material. We note that, while the solvent concentration is theoretically unbounded with the square-root singularity, the number of solvent molecules remains finite within a finite domain around the crack tip.

Next, the crack opening displacements are shown in Fig. 8, for the immersed and not-immersed cases with $\varepsilon_\infty = 10^{-3}$. The instantaneous opening profiles taken at $t/\tau = 10^{-4}$ are similar for both cases, and they agree closely with the LEFM prediction. Note that, subject to a prescribed far-field strain, the LEFM solution for the crack opening is independent of the elastic properties of the material [60]

$$\hat{u}_2(x_1) = 2\varepsilon_\infty \sqrt{a^2 - x_1^2} \quad (|x_1| \le a) \tag{4.11}$$

For the hydrogel specimens, the crack opening evolves with time due to solvent diffusion, and the two cases are different. For the immersed case (Fig. 8(*a*)), the crack first opens up and then gradually closes in. At the equilibrium state ($t/\tau = 10^5$), the opening profile is nearly identical to the instantaneous profile, also in agreement with the LEFM prediction. For the not-immersed case (Fig. 8(*b*)), however, the crack opens up continuously and attains an equilibrium profile different from the LEFM prediction. This behavior again suggests that the not-immersed hydrogel specimen cannot be treated as a homogenous elastic material, even for an infinitesimal far-field strain, because of solvent diffusion around the crack tip. Figure 8(*c*) shows the evolution of the maximum opening at the center of the crack, $\delta(t) = \hat{u}_2(x_1 = 0, t)$, for the immersed and the not-immersed hydrogel specimens. The equilibrium opening for the not-immersed case is about 50% larger than the LEFM prediction. On the other hand, the opening–closing behavior of the immersed hydrogel specimen reaches a maximum opening in the transient stage. It is found that the maximum crack opening depends on the size of the hydrogel specimen. With increasing specimen size, $h/a = 10$, 20, and 100, the maximum opening increases, and it takes longer time to reach the equilibrium opening. This suggests two competing effects due to solvent diffusion. In the early stage of evolution, the crack opens up due to solvent diffusion around the crack tip, including the outgoing diffusion across the crack faces. This stage is independent of the specimen size. In the later stage, the crack closes in as the solvent diffusion from the outer boundaries reaches the crack; the time for the incoming diffusion to reach the crack depends on the specimen size. The maximum crack opening is reached when the effect of incoming diffusion takes over. In contrast, for the not-immersed case, the diffusion occurs primarily around the crack, with a single time scale associated with the crack length.

The modified J-integral (J^*) in Eq. (2.24) is calculated for the stationary crack model by the domain integral in Eq. (2.27) as the driving force for straight-ahead crack growth. The path independence of the modified J-integral is shown in Fig. 9(*a*), where the domain integral is calculated for the immersed hydrogel specimen with increasing radius of the contour (C_1 in Fig. 2) at three time instants representing the instantaneous ($t/\tau = 10^{-4}$), transient ($t/\tau = 10^3$), and equilibrium ($t/\tau = 10^5$) states. The results for the not-immersed specimen are similar (not shown). In contrast,

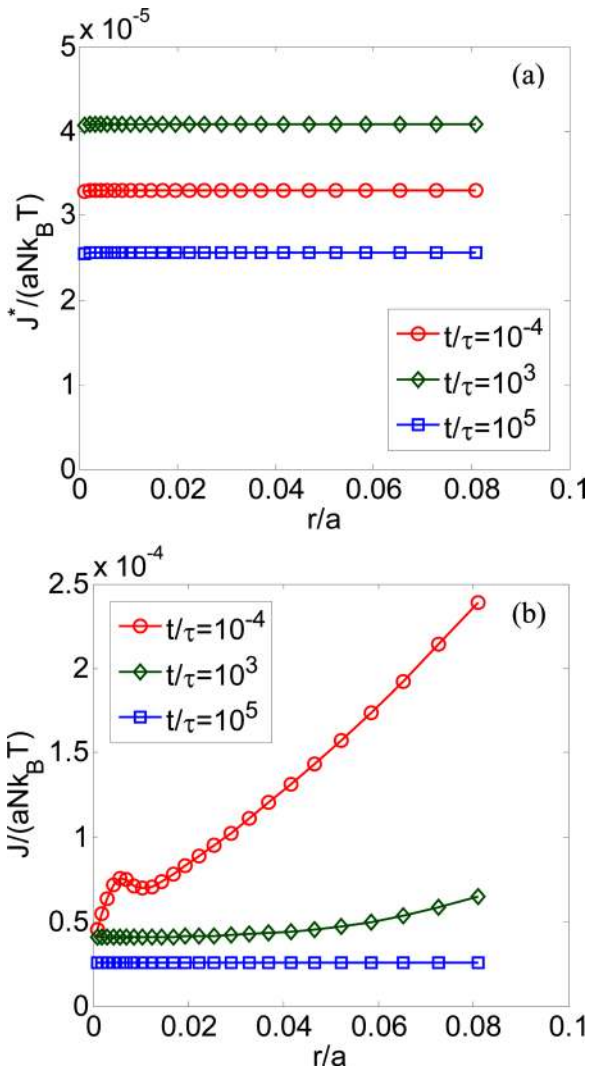

Fig. 9 (*a*) Path-independent J^*-integral and (*b*) the classical J-integral for the immersed hydrogel specimen ($\varepsilon_\infty = 10^{-3}$) at the instantaneous, transient, and equilibrium states. Here, r is the radius of the contour (C_1 in Fig. 2); the annular domain (A_2) is taken to be one ring of elements outside the contour for the domain integral calculations.

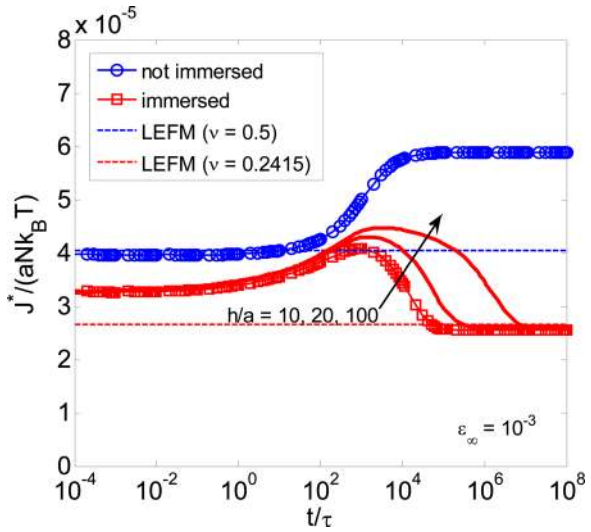

Fig. 10 J^* as a function of time for the immersed and not-immersed hydrogel specimens subject to a small far-field strain ($\varepsilon_\infty = 10^{-3}$). The effect of the specimen size is shown for the immersed case with $h/a = 10, 20$, and 100.

Fig. 9(*b*) shows the classic J-integral, calculated by the same domain integral but without the last term in Eq. (2.27). Evidently, the classic J-integral is path-dependent for the hydrogel specimen, except for the equilibrium state ($t/\tau = 10^5$). It is noted that the classic J-integral calculated with an infinitesimal contour radius ($A_1 \to 0$ in Fig. 2) approaches the modified J-integral closely, which can be expected from Eq. (2.24) with a vanishing volume integral on the right-hand side.

Figure 10 shows the evolution of J^* for the immersed and not-immersed hydrogel specimens subject to a small far-field strain ($\varepsilon_\infty = 10^{-3}$). The instantaneous responses for both cases are compared to LEFM with a Poisson's ratio, $\nu = 0.5$. With $K_I = \sigma_\infty\sqrt{\pi a}$, the instantaneous J-integral by LEFM is

$$J^*(t \to 0) = \lambda_0^2 \frac{(1-\nu^2)K_I^2}{E} = 4\pi N k_B T \varepsilon_\infty^2 \lambda_0 a \tag{4.12}$$

Note that the J^*-integral by definition is the energy release rate per unit area of crack in the reference configuration while the initial configuration of the hydrogel specimen has an isotropic swelling ratio λ_0. As shown in Fig. 10, while the calculated J^* agrees closely with Eq. (4.12) at the instantaneous limit for the not-immersed specimen, the agreement is poor for the immersed case. This is believed to be an effect of the boundary condition $\mu = 0$ for the immersed specimen, which imposes an instantaneous gradient of chemical potential in the crack tip elements. As a result, solvent diffusion occurs almost instantaneously (over the first time step) from the solvent inside the crack to the crack-tip elements, leading to a lower J^*.

While the J^*-integral increases monotonically with time for the not-immersed specimen, it increases slightly and then decreases for the immersed case. This behavior is similar to the evolution of crack opening shown in Fig. 8 for both cases. In addition, the effect of the specimen size is shown for the immersed case, where the peak J^* increases with increasing specimen size, a result of the two competing effects due to solvent diffusion as discussed earlier for crack opening. For the not-immersed case, the results are indistinguishable for different specimen sizes. After a

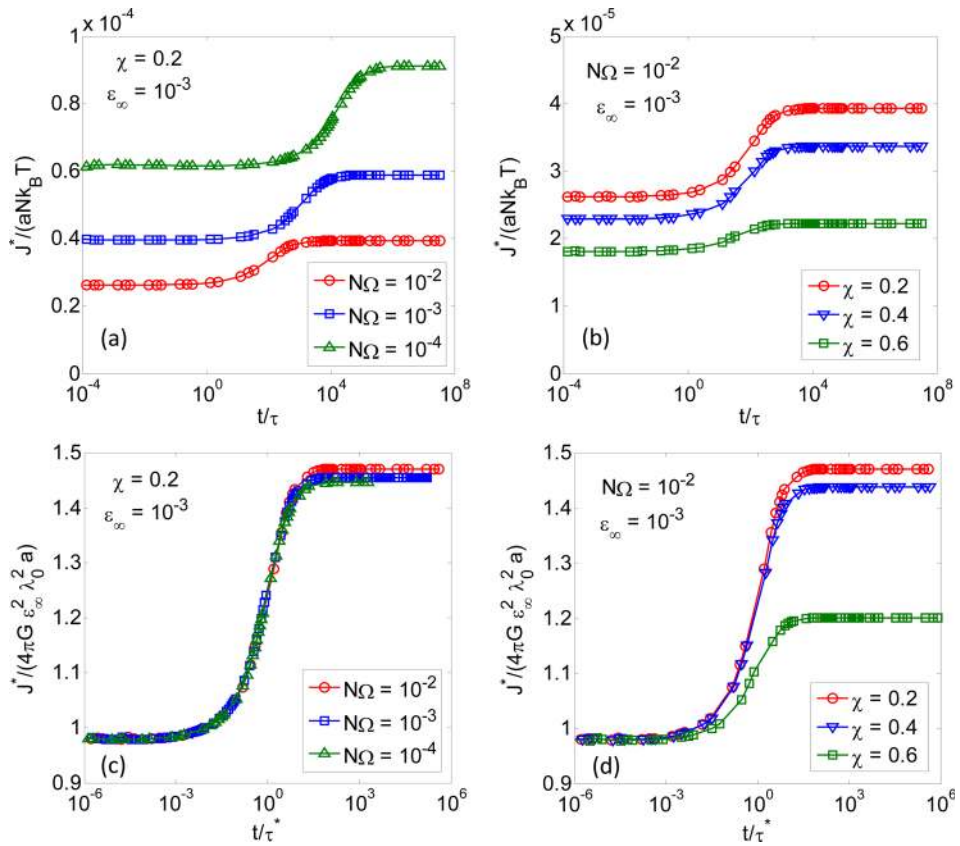

Fig. 11 Dependence of the J^*-integral on the material parameters for not-immersed hydrogel specimens under a small far-field strain ($\varepsilon_\infty = 10^{-3}$). (*a*) and (*b*) show the dependence on $N\Omega$ and χ, respectively. (*c*) and (*d*) The renormalized results using the instantaneous J^* in Eq. (4.12) and the poroelastic timescale, $\tau^* = a^2/D^*$, with the effective diffusivity in Eq. (4.14).

sufficiently long time, the J^*-integral saturates at an equilibrium value. For the immersed specimen, the equilibrium J^* agrees closely with the LEFM solution

$$J^*(t \to \infty) = \lambda_0^2 \frac{(1-\nu^2)K_I^2}{E} = \frac{2\pi}{1-\nu_\infty} N k_B T \varepsilon_\infty^2 \lambda_0 a \qquad (4.13)$$

where the Poisson's ratio ν_∞ is given in Eq. (4.10). With $\nu_\infty < 0.5$, the equilibrium J^* is lower than the instantaneous limit in Eq. (4.12). For the not-immersed specimen, however, the equilibrium J^* is higher. This is consistent with the calculations by Wang and Hong [33] who assumed similar boundary conditions to the not-immersed case, and the monotonic increase of J^* could lead to delayed fracture of gels [63]. Notably, while the J^*-integral can be related to the stress intensity factor by the LEFM relation at the instantaneous limit, the same relation does not hold at the equilibrium limit for the not-immersed case. The stress intensity factor obtained by the stress distributions (similar to Fig. 5) at the equilibrium limit is found to be nearly identical to the instantaneous limit [62], but the J^*-integrals are different at the two limits. This may be understood as a result of solvent diffusion around the crack tip where the solvent concentration (C) is inhomogeneous at the equilibrium limit. Moreover, while the chemical potential is homogeneous at equilibrium, it is not zero for the not-immersed case. As a result, the volume integral in Eq. (2.22) has a nonvanishing contribution to J^*, while the same integral vanishes in the instantaneous limit (homogeneous C) as well as in the equilibrium limit for the immersed case (zero μ).

The dependence of the J^*-integral on the material parameters of hydrogel is shown in Fig. 11 for the not-immersed specimens with $\varepsilon_\infty = 10^{-3}$; the dependence is similar for the immersed specimens (not shown). Both the instantaneous and equilibrium values of J^* depend on the two dimensionless parameters, $N\Omega$ and χ; the time scale of the evolution depends on them too. In Figs. 11(*c*) and 11(*d*), we rescale J^* with the instantaneous limit given by Eq. (4.12) and rescale the time using the poroelastic timescale, $\tau^* = a^2/D^*$, where the effective diffusivity is defined as [59]

$$D^* = \frac{2(1-\nu_\infty)(\lambda_0^3 - 1)N\Omega}{(1-2\nu_\infty)\lambda_0^4} D \qquad (4.14)$$

After rescaling, we note that: (1) the instantaneous J^* is well predicted by Eq. (4.12) in all cases; (2) the ratio between the equilibrium J^* and the instantaneous J^* is nearly independent of $N\Omega$, but decreases with increasing χ; and (3) the time scale for the transient evolution is captured effectively by the poroelastic timescale. Since the time-dependent J^* is a result of solvent diffusion within the hydrogel, the effect is expected to depend on the amount of solvent in the hydrogel. With increasing χ, the swelling ratio λ_0 decreases and the solvent concentration decreases so that the effect of solvent diffusion reduces, leading to smaller ratio between the equilibrium J^* and the instantaneous J^*. Moreover, with a small far-field strain ($\varepsilon_\infty = 10^{-3}$), the LEFM can be used to predict the instantaneous limit, and the linearized poroelastic properties can be used to predict a time scale for the transient behavior. However, these predictions are expected to become less satisfactory for larger far-field strains as discussed in Secs. 4.1.2 and 4.2.

4.1.2 Moderately Large Far-Field Deformations. Figure 12 shows the modified J-integrals for the immersed and not-immersed specimens under small to moderately large far-field strains. Here, the calculated J^* is normalized by the instantaneous limit based on LEFM as given by Eq. (4.12). While the overall trend is similar, the LEFM-based prediction becomes less accurate for a moderately large far-field strain ($\varepsilon_\infty = 0.1$); both the instantaneous J^* in the case of the not-immersed specimens and the equilibrium J^* in the case of the immersed specimens are lower than the LEFM predictions. This may be understood as a result of neo-Hookean nonlinear elasticity assumed as part of the constitutive model for the hydrogel (Eq. 3.2).

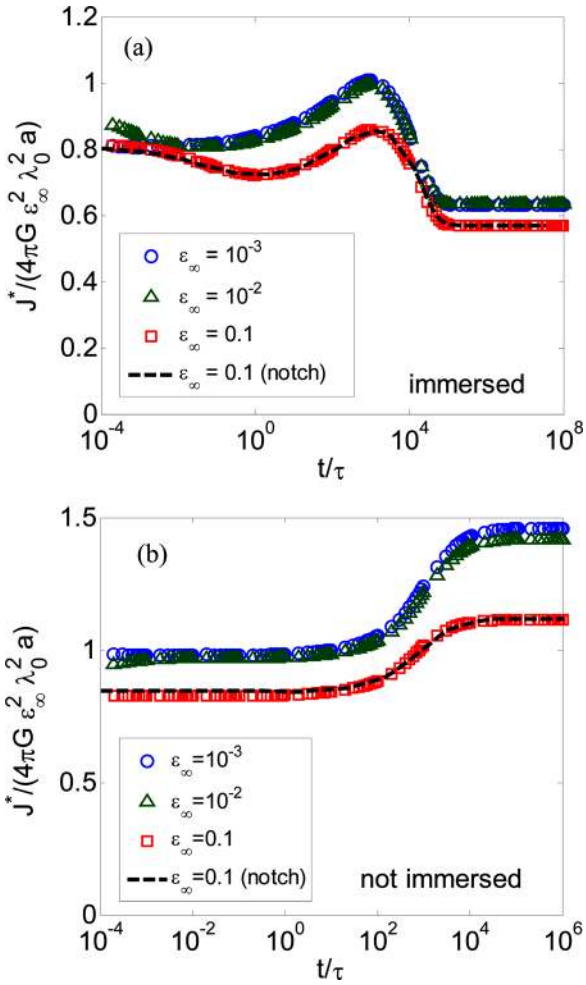

Fig. 12 Normalized J^* for immersed (*a*) and not-immersed (*b*) hydrogel specimens with increasing far-field strain. The results from the rounded notch model are compared to the sharp crack model for $\varepsilon_\infty = 0.1$.

Figure 13(*a*) shows the crack opening profiles for the immersed hydrogel specimen with $\varepsilon_\infty = 0.1$. Again, the opening–closing trend is similar to the small-strain case shown in Fig. 8. The effect of finite deformation is noticeable as the location of the crack tip shifts toward the center due to relatively large crack opening. As a result, the crack-tip elements are severely distorted in the sharp-crack model, which may cause numerical divergence for the finite element method. This issue can be resolved by using the rounded notch model as shown in Fig. 1(*b*), discussed further in Sec. 4.2.

4.2 Rounded Notch Crack Model. Figure 4(*b*) shows the mesh near the rounded-notch crack tip, with a small radius r_n ($r_n/a = 10^{-3}$). Similar crack models have been used previously to study fracture of elastic–plastic materials [52,53,64]. With a rounded notch, the calculation of the energy release rate using the J-integral must be modified to account for the contribution of the contour integral along the notch. Following Rice [53], the energy release rate is calculated by Eq. (2.24) with a surface integral around the notch (S_1 in Fig. 1(*b*)) and an integral over the enclosed volume (V_1). However, since the free energy density is nonzero in the initial state (before loading) and there is a finite gap across the notch, the same J^*-integral does not vanish in the initial state and should be subtracted from the calculation of the energy release rate, namely,

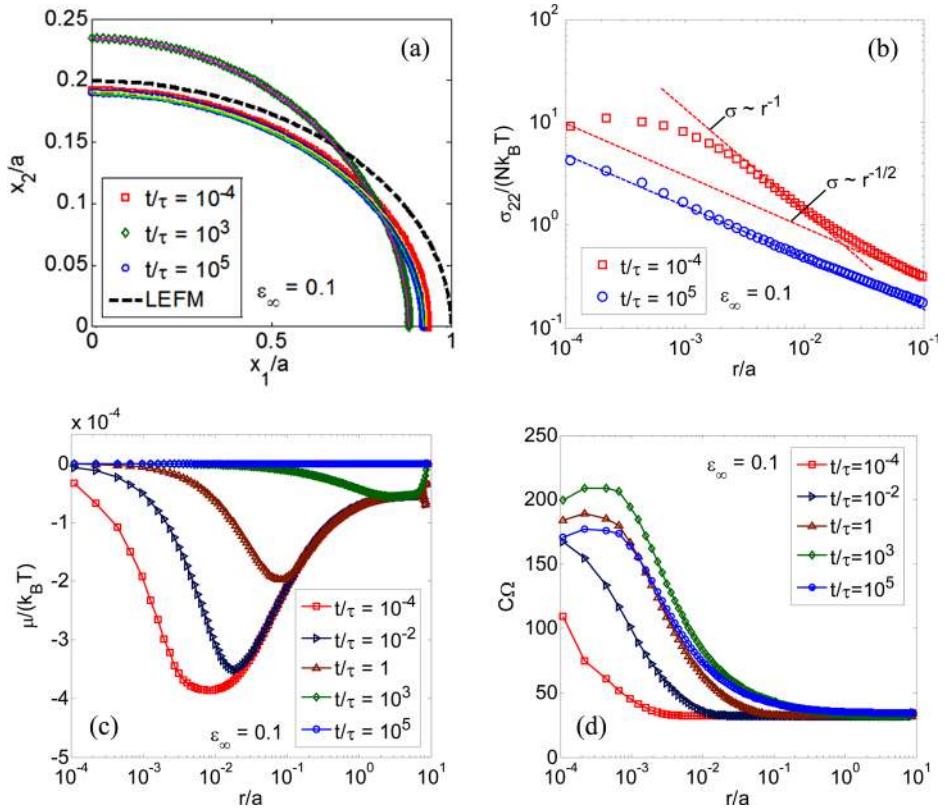

Fig. 13 (*a*) Crack opening profiles for an immersed hydrogel specimen under a moderately large far-field strain ($\varepsilon_\infty = 0.1$), from the sharp crack model (thin lines) and the rounded notch model (symbols); the dashed line shows the LEFM prediction. (*b*) Distribution of the Cauchy stress σ_{22} ahead of the crack tip in the instantaneous and equilibrium limits. (*c*) Evolution of the chemical potential and (*d*) the solvent concentration ahead of the crack tip.

$$J^*_{\text{notch}} = \int_{S_1} \left(\hat{U}N_1 - s_{iJ}N_J \frac{\partial x_i}{\partial X_1} \right) dS + \int_{V_1} \frac{\partial \mu}{\partial X_1} C dV - \left[\int_{S_1} \hat{U}N_1 dS \right]_{t=0} \tag{4.15}$$

where the initial state is assumed be stress free with a homogeneous chemical potential field. Equivalently, the energy release rate can be calculated by an integral over the surface of the rounded notch (S_2 in Fig. 1(*b*)), which is traction-free, and hence,

$$J^*_{\text{notch}} = \int_{-S_2} \hat{U}N_1 dS - \left[\int_{-S_2} \hat{U}N_1 dS \right]_{t=0} \tag{4.16}$$

In both Eqs. (4.15) and (4.16), the integrals in the initial state ($t = 0$, before loading) can be calculated analytically since the free energy density in the homogeneously swollen state can be obtained from Eq. (3.5) with $F_{iK} = \lambda_0 \delta_{iK}$ and $\mu = 0$.

The results from the rounded notch model are compared to the sharp crack model for a moderately large far-field strain of $\varepsilon_\infty = 0.1$. The crack opening profiles for the immersed hydrogel specimen are compared in Fig. 13(*a*), showing good agreement in the instantaneous, transient, and equilibrium states. The evolution of energy release rate (J^* or J^*_{notch}) is compared in Fig. 12 for both the immersed and not-immersed specimens, again with close agreement between the two crack models. In Fig. 13(*b*), the Cauchy stress σ_{22} ahead of the crack tip is plotted as a function of the distance from the crack tip at the instantaneous and equilibrium limits for an immersed hydrogel specimen. Although the crack opening profiles are nearly identical in the two limits (Fig. 13(*a*)), the stress distributions are quite different. The stress distribution in the equilibrium limit closely follows the square-root singularity ($\sigma \sim r^{-1/2}$) as predicted by LEFM, which however is not the case in the instantaneous limit. Theoretically, the instantaneous response of a hydrogel should be similar to an incompressible, hyperelastic material, for which a stronger singularity ($\sigma \sim r^{-1}$) has been predicted previously [65–67]. The numerical result at a very short time ($t/\tau = 10^{-4}$) shows a transition from the square-root singularity to the stronger singularity at roughly $r/a \sim 10^{-2}$ (Fig. 13(*b*)). This transition is consistent with the previous study on fracture of hyperelastic materials [66]; the same transition is not observable in the case of small far-field strain (Fig. 5), because the transition would occur at a much shorter distance ($r/a \sim \varepsilon_\infty^2$). Furthermore, Fig. 13(*b*) shows another transition at $r/a \sim 10^{-3}$, where the stress singularity becomes much weaker (almost nonsingular). This is not expected for the hyperelastic behavior at the instantaneous limit ($t \to 0$), but may be explained as a result of solvent diffusion. As shown in Figs. 13(*c*) and 13(*d*), even at $t/\tau = 10^{-4}$, both the chemical potential and solvent concentration have become inhomogeneous near the crack tip; hence, it is not exactly instantaneous per se. As the solvent concentration has increased significantly near the crack tip, the stress intensity very close to the crack tip ($r/a < 10^{-3}$) is reduced, because the material becomes softer with higher solvent concentration. Therefore, the stress distribution near the crack tip under a moderately large far-field strain is influenced by both hyperelasticity and solvent diffusion in the hydrogel specimen. On the other hand, the square-root singularity in the equilibrium limit may be a result of zero chemical potential although the solvent concentration is highly inhomogeneous around the crack tip (Fig. 13(*d*)); the corresponding energy release rate (J^*or J^*_{notch}) is lower than the LEFM prediction in Eq. (4.13) (see Fig. 12(*a*)).

As a final example, we consider a significantly large far-field strain $\varepsilon_\infty = 0.5$ for both the immersed and not-immersed hydrogel

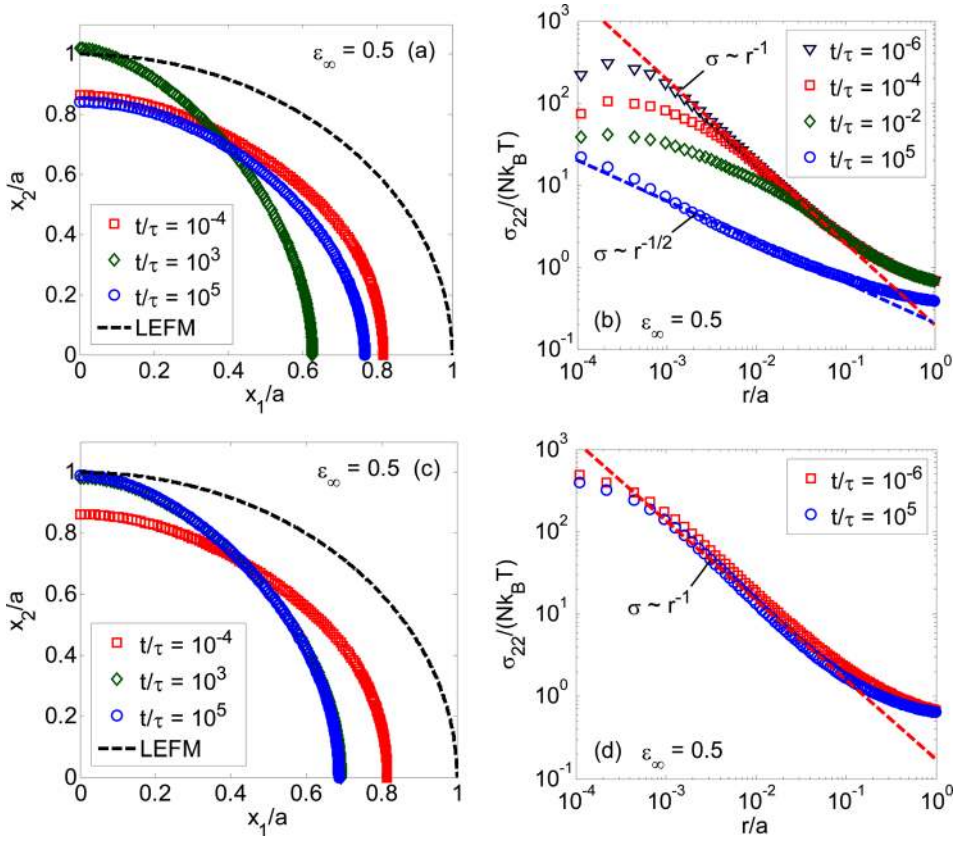

Fig. 14 Crack opening profiles and distributions of the Cauchy stress σ_{22} ahead of the crack tip under a large far-field strain ($\varepsilon_\infty = 0.5$). ((*a*) and (*b*)) For an immersed hydrogel specimen and ((*c*) and (*d*)) for a not-immersed hydrogel specimen.

specimens using the rounded notch model. In Fig. 14, the crack opening profiles are shown along with the stress distributions ahead of the crack tip. Of particular interest is the evolution of the stress distribution. For the immersed hydrogel specimen, the strong singularity ($\sigma \sim r^{-1}$) due to hyperelasticity is prominent in the early stage, with a transition to weaker singularity due to solvent diffusion near the crack tip (Fig. 14(*b*)). Eventually, the stress distribution approaches the square-root singularity ($\sigma \sim r^{-1/2}$) in the equilibrium limit. For the not-immersed hydrogel specimen, the stress distribution does not change significantly from the instantaneous to equilibrium, exhibiting the strong singularity ($\sigma \sim r^{-1}$) that becomes slightly weaker at the crack tip (Fig. 14(*d*)). The evolution of the modified J-integral is shown in Fig. 15. The overall behavior is similar to the small-strain behavior shown in Fig. 10, but the instantaneous J^* is considerably lower than the LEFM prediction for both the immersed and not-immersed specimens. The J-integral increases monotonically for the not-immersed case but remains lower than the LEFM prediction all the time. The transient energy release rate for the immersed hydrogel specimen is consistently lower than that for the not-immersed specimen under the same far-field strain.

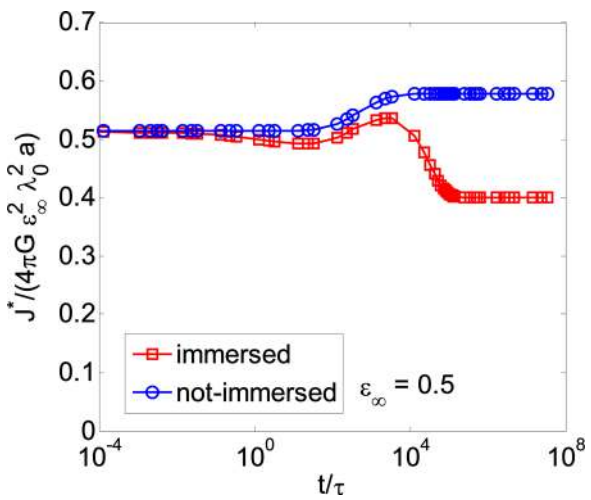

Fig. 15 Evolution of the modified *J*-integral for an immersed and a not-immersed hydrogel specimens under a large far-field strain ($\varepsilon_\infty = 0.5$)

5 Summary

The main results from the present study are summarized as follows.

(1) A thermodynamically consistent approach is presented for calculating the transient energy release rate for quasi-static crack growth in hydrogels based on a modified path-independent J-integral. The transient energy release rate takes into account the effect of solvent diffusion around the crack, separating the energy lost in diffusion from the energy available to drive crack growth.
(2) Assuming a specific material model for hydrogels with incompressible constituents, a nonlinear, transient finite element method is implemented for solving initial boundary value problems with coupled deformation and solvent diffusion in hydrogels. Numerical results are presented for center-cracked hydrogel specimens subject to remote tension by mode I displacement controlled loading.
(3) A sharp crack model is used for small far-field strains. The effects of solvent diffusion are studied for the hydrogel

specimens with different chemical boundary conditions, either immersed in a solvent or not-immersed. In both cases, the stress fields near the crack tip in the instantaneous and equilibrium limits compare closely with the LEFM prediction with appropriate Poisson's ratios. The transient energy release rate is a function of time, increasing monotonically for the not-immersed specimen. For the immersed specimen, the transient energy release rate reaches a peak and then decreases with time; the equilibrium energy release rate is lower than the instantaneous value.

(4) A rounded notch model is used for large far-field strains. In this case, the stress distributions around the crack tip exhibit a stronger singularity ($\sigma \sim r^{-1}$) due to hyperelasticity but transition to a weaker singularity near the crack tip due to solvent diffusion. The square-root stress singularity ($\sigma \sim r^{-1/2}$) is recovered at the equilibrium limit for the immersed specimen, but not for the nonimmersed specimen. The transient energy release rate as a function of time is similar to the small-strain behavior, but the value is considerably lower than the LEFM prediction in both the instantaneous and equilibrium limits.

As the thermodynamic driving force for crack growth, the transient energy release rate may be used to predict the critical condition for fracture. Assuming a critical energy release rate J_c^* in terms of the modified J-integral, crack growth may be predicted when $J^*(t) = J_c^*$. With $J^*(t)$ monotonically increasing for a not-immersed hydrogel specimen, delayed fracture [33,63] may be predicted if $J^*(t \to 0) < J_c^* < J^*(t \to \infty)$. For the immersed specimen, however, delayed fracture is unlikely since the peak energy release rate is close to the instantaneous value. However, the fracture criterion for hydrogels may be further complicated if the critical energy release rate depends on solvent concentration, for example, as a result of physical interactions between solvent molecules and the polymer network. Different fracture mechanisms may also lead to different fracture criteria for hydrogels [12–14,22], a subject to be further studied by combining the numerical model with experiments.

Acknowledgment

The authors gratefully acknowledge financial support by National Science Foundation (Grant No. CMMI-1200161). C.M.L. acknowledges the support from National Science Foundation (Grant No. CMMI-1068024).

Appendix A: Derivation of the Energy Release Rate

First, rewrite Eq. (2.14) as

$$\delta\Psi = \delta\Psi_V + \delta\Psi_T + \delta\Psi_\mu \tag{A1}$$

where

$$\delta\Psi_V = \int_{V_0} \left(\delta U - \frac{\partial \mu}{\partial X_K} \delta I_K \right) dV \tag{A2}$$

$$\delta\Psi_T = -\int_{S_T} (T_i \delta x_i) dS \tag{A3}$$

$$\delta\Psi_\mu = \int_{S_\mu} (\mu N_K \delta I_K) dS \tag{A4}$$

Here, we have ignored the body force and solvent injection source. The boundary S_T is a part of S_0 with specified tractions that do work by variation in displacements, and the boundary S_μ is a part of S_0 with specified chemical potential that do work by in/out flux of the solvent molecules.

Next, to derive the energy release rate with respect to a straight-ahead crack growth, consider a hydrogel body with a crack of length $\tilde{a}$ in the reference configuration and the same hydrogel body with a crack length $\tilde{a} + \delta\tilde{a}$. With the crack extension, the boundary of the body has changed to $S_0 + \delta S$, where δS is the new crack surface. Since the new crack surface is traction free, the work done by all tractions remains the same as Eq. (A3), which can be extended to an integral over S_0 (noting that $\delta x_i = 0$ on $S_0 - S_T$), namely,

$$\delta\Psi_T = -\int_{S_0} (T_i \delta x_i) dS \tag{A5}$$

Correspondingly, the work done by solvent flux is

$$\delta\Psi_\mu = \int_{S_\mu} (\mu N_K \delta I_K) dS + \int_{\delta S} (\mu N_K I_K) dS \tag{A6}$$

The second term on the right-hand side of Eq. (A6) vanishes for the two types of boundary conditions: (1) $\mu = 0$ on the crack faces for immersed specimens and (2) $N_K I_K = 0$ on the crack faces for not-immersed specimens. In either case, Eq. (A6) can be rewritten with an integral over S_0 (noting that $N_K \delta I_K = 0$ on $S_0 - S_\mu$), namely,

$$\delta\Psi_\mu = \int_{S_0} (\mu N_K \delta I_K) dS \tag{A7}$$

Therefore, the change of the total energy with respect to the crack length consists of three parts, given by Eqs. (A2), (A5), and (A7), which leads to Eq. (2.15).

Appendix B: Formulation of a Finite Element Method

Weak Form. The primary unknowns in the present problem are a vector field of displacement and a scalar field of chemical potential, $\mathbf{u}(\mathbf{X}, t)$ and $\mu(\mathbf{X}, t)$, which are coupled in general. Similar to the previous work [44], we obtain a weak form by using a pair of test functions, $\boldsymbol{\delta}\mathbf{u}(\mathbf{X})$ and $\delta\mu(\mathbf{X})$. Multiplying Eq. (2.3) by δu_i, integrating over V_0, and applying the divergence theorem, we obtain that

$$\int_{V_0} s_{iJ} \delta u_{i,J} dV = \int_{V_0} b_i \delta u_i dV + \int_{S_0} T_i \delta u_i dS \tag{B1}$$

Similarly, multiplying Eq. (2.5) by $\delta\mu$ and applying the divergence theorem, we obtain that

$$\int_{V_0} \frac{\partial C}{\partial t} \delta\mu dV - \int_{V_0} J_K \delta\mu_{,K} dV = \int_{V_0} r \delta\mu dV + \int_{S_0} i \delta\mu dS \tag{B2}$$

Hence, the weak form of the problem statement is to find $\mathbf{u}(\mathbf{X}, t)$ and $\mu(\mathbf{X}, t)$ such that the integral equations ((B1) and (B2)) are satisfied for any permissible test functions, $\{\boldsymbol{\delta}\mathbf{u}, \delta\mu\}$.

Time Integration. A backward Euler scheme is used to integrate Eq. (B2) over time

$$\int_{V_0} \frac{C^{t+\Delta t} - C^t}{\Delta t} \delta\mu dV - \int_{V_0} J_K^{t+\Delta t} \delta\mu_{,K} dV = \int_{V_0} r^{t+\Delta t} \delta\mu dV + \int_{S_0} i^{t+\Delta t} \delta\mu dS \tag{B3}$$

where the superscripts indicate quantities at the current time step $(t + \Delta t)$ or the previous step (t). Combining Eq. (B3) with Eq. (B1), we obtain that

$$\int_{V_0} \left(s_{iJ}\delta u_{i,J} - C\delta\mu + \Delta t J_K \delta\mu_{,K}\right) dV = \int_{V_0} (b_i \delta u_i - r\Delta t\delta\mu - C^t\delta\mu) dV + \int_{S_0} T_i \delta u_i dS - \int_{S_0} i\Delta t\delta\mu dS \tag{B4}$$

where the superscript $(t+\Delta t)$ is omitted for all the terms at the current time step and C^t is the solvent concentration at the previous time step.

Spatial Discretization. Next, the displacement and chemical potential are discretized through interpolation in the domain of interest

$$\mathbf{u} = \mathbf{N}^u \mathbf{u}^n \text{ and } \mu = \mathbf{N}^\mu \boldsymbol{\mu}^n \tag{B5}$$

where $\mathbf{N}^u$ and $\mathbf{N}^\mu$ are the shape functions, $\mathbf{u}^n$ and $\boldsymbol{\mu}^n$ are the nodal values of the displacement and chemical potential, respectively. The test functions are discretized in the same way

$$\boldsymbol{\delta}\mathbf{u} = \mathbf{N}^u \boldsymbol{\delta}\mathbf{u}^n \text{ and } \delta\mu = \mathbf{N}^\mu \boldsymbol{\delta}\boldsymbol{\mu}^n \tag{B6}$$

The stress, solvent concentration, and flux are evaluated at integration points, depending on the gradients of the displacement and chemical potential via the constitutive relations. Taking the gradient of Eq. (B5), we obtain that

$$\nabla\mathbf{u} = \mathbf{F} - \mathbf{I} = \nabla\mathbf{N}^u\mathbf{u}^n = \mathbf{B}^u\mathbf{u}^n \tag{B7}$$

$$\nabla\mu = \nabla\mathbf{N}^\mu\boldsymbol{\mu}^n = \mathbf{B}^\mu\boldsymbol{\mu}^n \tag{B8}$$

where $\mathbf{B}^u$ and $\mathbf{B}^\mu$ are the gradients of the shape functions. In this formulation, we have allowed the use of different shape functions to interpolate the displacement and chemical potential fields, which is necessary for the implementation of Taylor–Hood elements as discussed in the previous study [44].

After the spatial discretization, invoking the arbitrariness of the test functions, the weak form in Eq. (B4) can be expressed as a system of nonlinear equations,

$$\mathbf{n}(\mathbf{d}) = \mathbf{f} \tag{B9}$$

where $\mathbf{d} = \begin{bmatrix} \mathbf{u}^n \\ \boldsymbol{\mu}^n \end{bmatrix}$. More specifically, the individual contributions to Eq. (B9) are

$$\begin{aligned} n_i^{u,M} &= \int_{V_0} s_{iJ} B_J^{u,M} dV \\ n^{\mu,M} &= \int_{V_0} \left(-CN^{\mu,M} + \Delta t J_K B_K^{\mu,M}\right) dV \end{aligned} \tag{B10}$$

$$\begin{aligned} f_i^{u,M} &= \int_{V_0} b_i N^{u,M} dV + \int_{S_0} T_i N^{u,M} dS \\ f^{\mu,M} &= \int_{V_0} (r\Delta t - C^t) N^{\mu,M} dV - \int_{S_0} i\Delta t N^{\mu,M} dS \end{aligned} \tag{B11}$$

where the superscript M refers to the node and the subscript in B_J^u refers to the direction in which the derivative is taken.

Newton–Raphson Method. The system of nonlinear equations in Eq. (B9) is solved iteratively using the Newton–Raphson method at each time step. In particular, the procedure requires calculation of the tangent Jacobian matrix at each iteration, namely,

$$\left.\frac{\partial \mathbf{n}}{\partial \mathbf{d}}\right|_{\mathbf{d}_i} = \begin{bmatrix} \mathbf{K}^{\mathbf{uu}} & \mathbf{K}^{\mathbf{u}\boldsymbol{\mu}} \\ \mathbf{K}^{\boldsymbol{\mu}u} & \mathbf{K}^{\boldsymbol{\mu}\boldsymbol{\mu}} \end{bmatrix} \tag{B12}$$

where for each pair of nodes (N, M) and degrees of freedom (i,k), the individual contributions in the matrix can be calculated using the explicit expression of the Legendre transformation of the free energy density in Eq. (3.5). As discussed in Ref. [44], although the tangent Jacobian matrix is asymmetric in general, a symmetric tangent Jacobian matrix can be used as an approximation for computational efficiency.

References

[1] Jagur-Grodzinski, J., 2006, "Polymers for Tissue Engineering, Medical Devices, and Regenerative Medicine. Concise General Review of Recent Studies," Polym. Adv. Technol., **17**(6), pp. 395–418.
[2] Drury, J. L., and Mooney, D. J., 2003, "Hydrogels for Tissue Engineering: Scaffold Design Variables and Applications," Biomaterials, **24**(24), pp. 4337–4351.
[3] Suciu, A. N., Iwatsubo, T., Matsuda, M., and Nishino, T., 2004, "A Study Upon Durability of the Artificial Knee Joint With PVA Hydrogel Cartilage," JSME Int. J. Ser. C, **47**(1), pp. 199–208.
[4] Luo, Y., and Shoichet, M. S., 2004, "A Photolabile Hydrogel for Guided Three-Dimensional Cell Growth and Migration," Nat. Mater., **3**(4), pp. 249–253.
[5] Discher, D. E., Mooney, D. J., and Zandstra, P. W., 2009, "Growth Factors, Matrices, and Forces Combine and Control Stem Cells," Science, **324**(5935), pp.1673–1677.
[6] Qiu, Y., and Park, K., 2001, "Environment-Sensitive Hydrogels for Drug Delivery," Adv. Drug Delivery Rev., **53**(3), pp. 321–339.
[7] Calvert, P., 2009, "Hydrogels for Soft Machines," Adv. Mater., **21**(7), pp. 743–756.
[8] Dong, L., Agarwal, A. K., Beebe, D. J., and Jiang, H. R., 2006, "Adaptive Liquid Microlenses Activated by Stimuli-Responsive Hydrogels," Nature, **442**(7102), pp. 551–554.
[9] Keplinger, C., Sun, J.-Y., Foo, C. C., Rothemund, P., Whitesides, G. M., and Suo, Z., 2013, "Stretchable, Transparent, Ionic Conductors," Science, **341**(6149), pp. 984–987.
[10] Kong, H. J., Wong, E., and Mooney, D. J., 2003, "Independent Control of Rigidity and Toughness of Polymeric Hydrogels," Macromolecules, **36**(12), pp. 4582–4588.
[11] Henderson, K. J., Zhou, T. C., Otim, K. J., and Shull, K. R., 2010, "Ionically Cross-Linked Triblock Copolymer Hydrogels With High Strength," Macromolecules, **43**(14), pp. 6193–6201.
[12] Baumberger, T., Caroli, C., and Martina, D., 2006, "Fracture of a Biopolymer Gel as a Viscoplastic Disentanglement Process," Eur. Phys. J. E, **21**(1), pp. 81–89.
[13] Baumberger, T., Caroli, C., and Martina, D., 2006, "Solvent Control of Crack Dynamics in a Reversible Hydrogel," Nat. Mater., **5**(7), pp. 552–555.
[14] Baumberger, T., and Ronsin, O., 2010, "Cooperative Effect of Stress and Ion Displacement on the Dynamics of Cross-Link Unzipping and Rupture of Alginate Gels," Biomacromolecules, **11**(6), pp. 1571–1578.
[15] Tanaka, Y., Fukao, K., and Miyamoto, Y., 2000, "Fracture Energy of Gels," Eur. Phys. J. E, **3**(4), pp. 395–401.
[16] Simha, N. K., Carlson, C. S., and Lewis, J. L., 2003, "Evaluation of Fracture Toughness of Cartilage by Micropenetration," J. Mater. Sci.: Mater. Med., **15**(5), pp. 631–639.
[17] Gamonpilas, C., Charalambides, M. N., and Williams, J. G., 2009, "Determination of Large Deformation and Fracture Behavior of Starch Gels From Conventional and Wire Cutting Experiments," J. Mater. Sci., **44**(18), pp. 4976–4986.
[18] Forte, A. E., D'Amico, F., Charalambides, M. N., Dini, D., and Williams, J. G., 2015, "Modelling and Experimental Characterisation of the Rate Dependent Fracture Properties of Gelatine Gels," Food Hydrocolloids, **46**, pp. 180–190.
[19] Kwon, H. J., Rogalsky, A. D., and Kim, D.-W., 2011, "On the Measurement of Fracture Toughness of Soft Biogel," Polym. Eng. Sci., **51**(6), pp. 1078–1086.
[20] Gong, J. P., 2010, "Why are Double Network Hydrogels so Tough?," Soft Matter, **6**(12), pp. 2583–2590.
[21] Sun, J.-Y., Zhao, X., Illeperuma, W. R. K., Chaudhuri, O., Oh, K. H., Mooney, D. J., Vlassak, J. J., and Suo, Z., 2012, "Highly Stretchable and Tough Hydrogels," Nature, **489**(7414), pp. 133–136.
[22] Zhao, X., 2014, "Multi-Scale Multi-Mechanism Design of Tough Hydrogels: Building Dissipation Into Stretchy Networks," Soft Matter, **10**(5), pp. 672–687.
[23] Hu, Y., and Suo, Z., 2012, "Viscoelasticity and Poroelasticity in Elastomeric Gels," Acta Mech. Solida Sin., **25**(5), pp. 441–457.
[24] Zhao, X., Huebsch, N. D., Mooney, D. J., and Suo, Z., 2010, "Stress-Relaxation Behavior in Gels With Ionic and Covalent Crosslinks," J. Appl. Phys., **107**(6), p. 063509.
[25] Hu, Y., Chen, X., Whitesides, G. M., Vlassak, J. J., and Suo, Z., 2011, "Indentation of Polydimethylsiloxane Submerged in Organic Solvents," J. Mater. Res., **26**(6), pp. 785–795.
[26] Galli, M., Fornasiere, E., Gugnoni, J., and Oyen, M. L., 2011, "Poroviscoelastic Characterization of Particle-Reinforced Gelatin Gels Using Indentation and Homogenization," J. Mech. Behav. Biomed. Mater., **4**(4), pp. 610–617.
[27] Knauss, W. G., 1973, "The Mechanics of Polymer Fracture," ASME Appl. Mech. Rev., **26**, pp. 1–17.
[28] Schapery, R. A., 1975, "A Theory of Crack Initiation and Growth in Viscoelastic Media," Int. J. Fract., **11**(1), pp. 141–159.

[29] Schapery, R. A., 1975, "A Theory of Crack Initiation and Growth in Viscoelastic Media II. Approximate Methods of Analysis," Int. J. Fract., **11**(3), pp. 369–388.
[30] Schapery, R. A., 1975, "A Theory of Crack Initiation and Growth in Viscoelastic Media," Int. J. Fract., **11**(4), pp. 549–562.
[31] Schapery, R. A., 1984, "Correspondence Principles and a Generalized J Integral for Large Deformation and Fracture Analysis of Viscoelastic Media," Int. J. Fract., **25**(3), pp. 195–223.
[32] Hui, C. Y., Long, R., and Ning, J., 2013, "Stress Relaxation Near the Tip of a Stationary Mode I Crack in a Poroelastic Solid," ASME J. Appl. Mech., **80**(2), p. 021014.
[33] Wang, X., and Hong, W., 2012, "Delayed Fracture in Gels," Soft Matter, **8**(31), pp. 8171–8178.
[34] Zhang, J., An, Y., Yazzie, K., Chawla, N., and Jiang, H., 2012, "Finite Element Simulation of Swelling-Induced Crack Healing in Gels," Soft Matter, **8**(31), pp. 8107–8112.
[35] Rice, J. R., and Cleary, M. P., 1976, "Some Basic Stress Diffusion Solutions for Fluid-Saturated Elastic Porous Media With Compressible Constituents," Rev. Geophys., **14**(2), pp. 227–241.
[36] Ruina, A., 1978, "Influence of Coupled Deformation-Diffusion Effects on the Retardation of Hydraulic Fracture," 19th U.S. Symposium on Rock Mechanics, Reno, NV, May 1–3.
[37] Detournay, E., and Cheng, A. H.-D., 1991, "Plane Strain Analysis of a Stationary Hydraulic Fracture in a Poroelastic Medium," Int. J. Solids Struct., **27**(13), pp. 1645–1662.
[38] Adachi, J. I., and Detournay, E., 2008, "Plane Strain Propagation of a Hydraulic Fracture in a Permeable Rock," Eng. Fract. Mech., **75**(16), pp. 4666–4694.
[39] Kishimoto, K., Aoki, S., and Sakata, M., 1980, "On the Path Independent Integral-J," Eng. Fract. Mech., **13**(4), pp. 841–850.
[40] Chien, N., and Herrmann, G., 1996, "Conservation Laws for Thermo or Poroelasticity," ASME J. Appl. Mech., **63**(2), pp. 331–336.
[41] Yang, F., Wang, J., and Chen, D., 2006, "The Energy Release Rate for Hygrothermal Coupling Elastic Materials," Acta Mech. Sin., **22**(1), pp. 28–33.
[42] Gao, Y. F., and Zhou, M., 2013, "Coupled Mechano-Diffusional Driving Forces for Fracture in Electrode Materials," J. Power Sources, **230**, pp. 176–193.
[43] Haftbaradaran, H., and Qu, J., 2014, "A Path-Independent Integral for Fracture of Solids Under Combined Electrochemical and Mechanical Loadings," J. Mech. Phys. Solids, **71**, pp. 1–14.
[44] Bouklas, N., Landis, C. M., and Huang, R., 2015, "A Nonlinear, Transient Finite Element Method for Coupled Solvent Diffusion and Large Deformation of Hydrogels," J. Mech. Phys. Solids, **79**, pp. 21–43.
[45] Dolbow, J., Fried, E., and Ji, H., 2004, "Chemically Induced Swelling of Hydrogels," J. Mech. Phys. Solids, **52**(1), pp. 51–84.
[46] Hong, W., Zhao, X., Zhou, J., and Suo, Z., 2008, "A Theory of Coupled Diffusion and Large Deformation in Polymeric Gels," J. Mech. Phys. Solids, **56**(5), pp. 1779–1793.
[47] Duda, F. P., Souza, A. C., and Fried, E., 2010, "A Theory for Species Migration in a Finitely Strained Solid With Application to Polymer Network Swelling," J. Mech. Phys. Solids, **58**(4), pp. 515–529.
[48] Chester, S. A., and Anand, L., 2010, "A Coupled Theory of Fluid Permeation and Large Deformations for Elastomeric Materials," J. Mech. Phys. Solids, **58**(11), pp. 1879–1906.
[49] Wang, X., and Hong, W., 2012, "A Visco-Poroelastic Theory for Polymeric Gels," Proc. R. Soc. London, Ser. A: Math. Phys. Eng. Sci., **468**(2148), pp. 3824–3841.
[50] Prigogine, I., 1968, *Introduction to Thermodynamics of Irreversible Processes*, Wiley, New York.
[51] Coleman, B. D., and Noll, W., 1963, "The Thermodynamics of Elastic Materials With Heat Conduction and Viscosity," Arch. Ration. Mech. Anal., **13**(1), pp. 167–178.
[52] Rice, J. R., 1968, "A Path Independent Integral and the Approximate Analysis of Strain Concentration by Notches and Cracks," ASME J. Appl. Mech., **35**(2), pp. 379–386.
[53] Rice, J. R., 1968, *Mathematical Analysis in the Mechanics Fracture. Fracture: An Advanced Treatise*, Vol. 2, Academic, New York, pp. 191–311.
[54] Li, F. Z., Shih, C. F., and Needleman, A., 1985, "A Comparison of Methods for Calculating Energy Release Rates," Eng. Fract. Mech., **21**(2), pp. 405–421.
[55] Murad, M. A., and Loula, A. F., 1994, "On Stability and Convergence of Finite Element Approximations of Biot's Consolidation Problem," Int. J. Numer. Meth. Eng., **37**(4), pp. 645–667.
[56] Wan, J., 2002, "Stabilized Finite Element Methods for Coupled Geomechanics and Multiphase Flow," Ph.D. dissertation, Stanford University, Stanford, CA.
[57] Phillips, P. J., and Wheeler, M. F., 2009, "Overcoming the Problem of Locking in Linear Elasticity and Poroelasticity: An Heuristic Approach," Comput. Geosci., **13**(1), pp. 5–12.
[58] Taylor, C., and Hood, P., 1973, "A Numerical Solution of the Navier–Stokes Equations Using the Finite Element Technique," Comput. Fluids, **1**(1), pp. 73–100.
[59] Bouklas, N., and Huang, R., 2012, "Swelling Kinetics of Polymer Gels: Comparison of Linear and Nonlinear Theories," Soft Matter, **8**(31), pp. 8194–8203.
[60] Broberg, K. B., 1999, *Cracks and Fracture*, Academic, San Diego, CA.
[61] Yoon, J., Cai, S., Suo, Z., and Hayward, R. C., 2010, "Poroelastic Swelling Kinetics of Thin Hydrogel Layers: Comparison of Theory and Experiment," Soft Matter, **6**(23), pp. 6004–6012.
[62] Bouklas, N., 2014, "Modelling and Simulation of Hydrogels With Coupled Solvent Diffusion and Large Deformation," Ph.D. dissertation, The University of Texas at Austin, Austin, TX.
[63] Bonn, D., Kellay, H., Prochnow, M., Ben-Djemiaa, K., and Meunier, J., 1998, "Delayed Fracture of an Inhomogeneous Soft Solid," Science, **280**(5361), pp. 265–267.
[64] McMeeking, R. M., 1977, "Finite Deformation Analysis of Crack-Tip Opening in Elastic–Plastic Materials and Implications for Fracture," J. Mech. Phys. Solids, **25**(5), pp. 357–381.
[65] Geubelle, P. H., 1995, "Finite Deformation Effects in Homogeneous and Interfacial Fracture," Int. J. Solids Struct., **32**(6–7), pp. 1003–1016.
[66] Krishnan, V. R., Hui, C. Y., and Long, R., 2008, "Finite Strain Crack Tip Fields in Soft Incompressible Elastic Solids," Langmuir, **24**(24), pp. 14245–14253.
[67] Bouchbinder, E., Livne, A., and Fineberg, J., 2009, "The 1/r Singularity in Weakly Nonlinear Fracture Mechanics," J. Mech. Phys. Solids, **57**(9), pp. 1568–1577.